Reconstruction of the 1908 Messina gravity flow (central Mediterranean Sea) from geophysical and sedimentological data

I. Schulten [a,*], A. Micallef [a], S. Krastel [b], M. Urlaub [c], M.-A. Gutscher [d], H. Kopp [c]

[a] Marine Geology and Seafloor Surveying, University of Malta, Msida, Malta
[b] Kiel University, Kiel, Germany
[c] GEOMAR Helmholtz Centre for Ocean Research Kiel, Kiel, Germany
[d] Geo-Ocean, Univ. Brest, CNRS, Ifremer, Brest, France

ARTICLE INFO

ABSTRACT

Earthquakes, tsunamis and gravity flows are common processes offshore Eastern Sicily and pose a significant hazard to coastal communities and infrastructure. The 1908 Messina earthquake and tsunami resulted in >60,000 casualties. It caused a large turbidity current, which broke the Malta-Zante telegraph cable. Yet, this gravity flow remains poorly characterised in terms of its route and flow behaviour. A comprehensive analysis of multibeam echosounder data, sub-bottom profiles, and sediment cores has been carried out to improve our understanding about gravity flow activity within conduit systems of the western Ionian Basin to reconstruct the characteristics of the 1908 sediment flow (e.g., erosion, velocity, source region). Three main canyon-channel systems can be distinguished within the study area. The easternmost system (C3) appears to be the most active in terms of sediment transport. There are numerous erosional and depositional bedforms, including large-scale scours (>100 m-long), turbidite sediment waves and channel wall collapses that are not overprinted by younger events. The other two canyon-channel systems (C1, C2) do not show many bedforms indicative of repeated and recent gravity flow activity. Indeed, the transport of the majority of sediment discharged into the western system (C1) is limited to <25 km downslope from the continental slope, while the central system (C2) facilitates sediment deposition from gravity flows. C3 is, thus, suggested to have been the main passageway of the 1908 sediment flow. It also leads directly to two of three cable break locations. The most likely source areas for the gravity flow are north-eastern Sicily and southern Calabria. Bedforms indicate a flow thickness of >170 m along the upper channel portion of C3 and > 140 m along its lower portion close to the cable breaks. An average flow velocity of 5.6 to 6.3 ms^{-1} is reconstructed, given the timing of the breaks and length of the canyon-channel system. The flow may have locally decelerated and accelerated while bypassing morphologic highs and knick-points. These new findings significantly improve our understanding of the 1908 gravity flow (e.g., passageways, depositional/erosional behaviour, thickness, velocity) and provide important insights into gravity flow events in general, especially those with a large run-out. This knowledge is needed to assess potential hazards associated with these events.

1. Introduction

Sediment gravity flows are some of the most important geological processes on Earth (Mosher et al., 2010; Mountjoy et al., 2018). These laminar to turbulent suspended density flows transport large quantities of sediment from continental margins to deep sea basins (Talling et al., 2012). They largely influence canyon and channel development, and play a key role in the development of sedimentary basins and facies distribution (Talling et al., 2013; Mountjoy et al., 2018; Stevenson et al., 2018). They also pose a geohazard to seafloor infrastructure such as telecommunication cables, as documented during the 1929 Grand Banks event (Heezen and Ewing, 1952; Piper et al., 1999), the 2003 Boumerdes Algeria earthquake (Babonneau et al., 2017) and the 2006 Pingtung Earthquake off SW Taiwan (Hsu et al., 2008). It has further been suggested that gravity flows may contribute to tsunami generation (Assier-Rzadkieaicz et al., 2000; Fine et al., 2005). In spite of their significance, sediment gravity flows remain poorly studied and understood, especially in terms of their flow properties and evolution and the spatial

variability of erosional and depositional processes. Various processes (e. g., earthquakes, submarine slides, floods, storms, tsunamis, anthropogenic activities) are known to trigger sediment gravity flows (e.g., Piper et al., 1999; Arai et al., 2013; Talling, 2014). It is, however, difficult to measure and monitor gravity flows in situ, as it is nearly impossible to predict when and where these events occur (Paull et al., 2003; Hage et al., 2018, 2019; Mountjoy et al., 2018; Clare et al., 2021; Talling et al., 2022). Hence, flow properties of large gravity flows are mainly

reconstructed based on the analysis of their deposits and modelling (e.g., Meiburg and Kneller, 2010; Talling et al., 2012; Stevenson et al., 2018).

A well-known historic event is the 1908 Messina turbidity current in the western Ionian Basin, offshore eastern Sicily, which is one of the most seismically active areas of the Mediterranean Sea (Ryan and Heezen, 1965) (Fig. 1A). A M$_w$7.1 earthquake on 28 December 1908 at 5:21 (local time), which caused >60,000 casualties and a tsunami, is known to have triggered the Messina turbidity current (Omori, 1909;
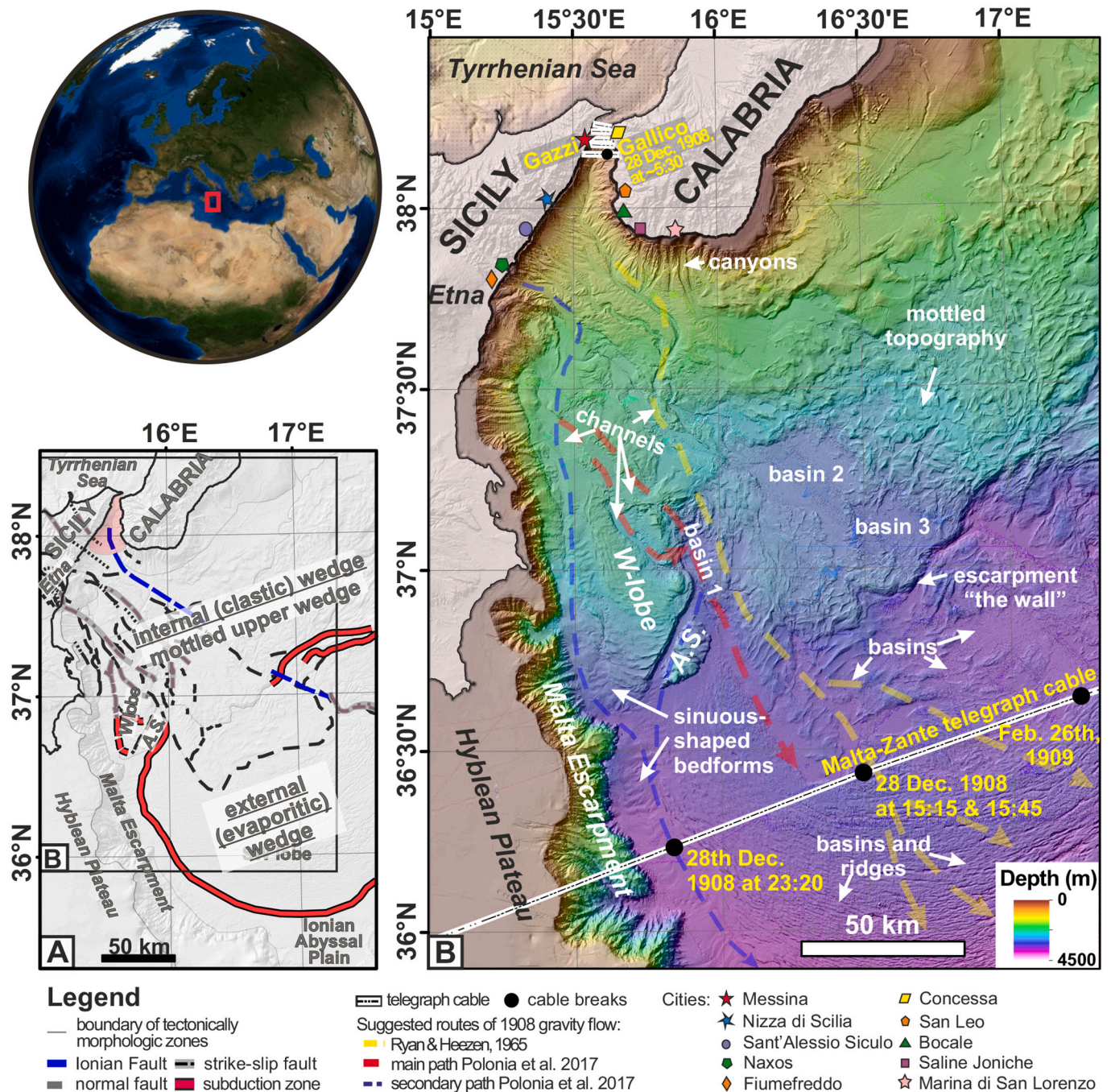

Fig. 1. Bathymetric maps highlighting the research area of this study, the western Ionian Basin. Prominent tectonic features in this region as a result of the active Calabrian subduction are highlighted in (A). Location of (A) is shown in the globe, which was created using ArcGlobe. Geomorphological features and the location of telegraph cables in 1908 (white-dotted line) and cable breaks (black circles) are shown in (B) (black box in (A)), which is the defined research area of this study. Acronyms W-lobe stands for the separated western lobe of the Calabrian Accretionary Wedge and A.S. for Alfeo Seamount. The transparent red polygon in (A) indicates the location of Messina Straits. The tectonic map is modified from Gutscher et al. (2016, 2017). Note: symbols indicating the location of various cities shown in (B) will be relevant for the results sections. (For interpretation of the references to colour in this figure legend, the reader is referred to the web version of this article.)

Ryan and Heezen, 1965; Tinti and Armigliato, 2003). The source of both the earthquake and tsunami is argued to be somewhere in the Messina Straits, but remains highly debated in the literature (e.g., Tinti and Armigliato, 2003; Billi et al., 2008; Argnani et al., 2009a; Barreca et al., 2021). Tsunami simulations based on proposed earthquake faults do not match observations (e.g., Tinti and Armigliato, 2003; Billi et al., 2008). A submarine landslide has been suggested to have contributed to tsunami generation (e.g., Billi et al., 2008; Favalli et al., 2009; Schambach et al., 2020), but such a contribution of a landslide is doubted by others (Argnani et al., 2009b; Gross et al., 2014). The event severed two telegraph cables, which are thought to have been the result of the gravity flow (Fig. 1B) (Ryan and Heezen, 1965) that was either caused by the earthquake directly or by one or several submarine landslides. The Gallico-Gazzi cable in the northern part of the Messina Straits broke at the time of the earthquake (Fig. 1B) (Ryan and Heezen, 1965). Three additional cable breaks were recorded across the Malta-Zante telegraph cable up to 18 h after the earthquake: one at 15:15 in the external Calabrian accretionary wedge (CAW) followed by a second break at 15:45 in the same location (Fig. 1B) (Ryan and Heezen, 1965). The third

break occurred at 23:20 closer to the Malta Escarpment (Fig. 1B) (Ryan and Heezen, 1965).

Since the first detailed description by Ryan and Heezen (1965), sediment cores showing evidence for the 1908 turbidity current have been collected from the western Ionian Basin (Fig. 2A). The turbidite is found in cores from a *syn*-tectonic basin located between the internal and external CAW and in proximity to the Ionian Abyssal Plain (IAP) (Fig. 2A) (Polonia et al., 2013, 2017, 2021). The distribution of the cable breaks, approximate location of the earthquake, and mineral composition of sediments in the cores allowed a first estimate of the source area, extent, flow direction and speed of the 1908 gravity flow (Ryan and Heezen, 1965; Polonia et al., 2013, 2017, 2021). Ryan and Heezen (1965) suggested an average flow velocity of ~6.2 ms^{-1} assuming the source to be west of Gallico (Southern Calabria) within the Messina Straits (Fig. 1B). Polonia et al. (2021) concluded that the gravity flow involved multiple source areas and suggested the seafloor offshore Mt. Etna (north-eastern Sicily) and southern Calabria, although no specific location is provided. They identified a canyon system southeast from Mt. Etna as the main passageway (Fig. 1B) (Polonia et al., 2017).
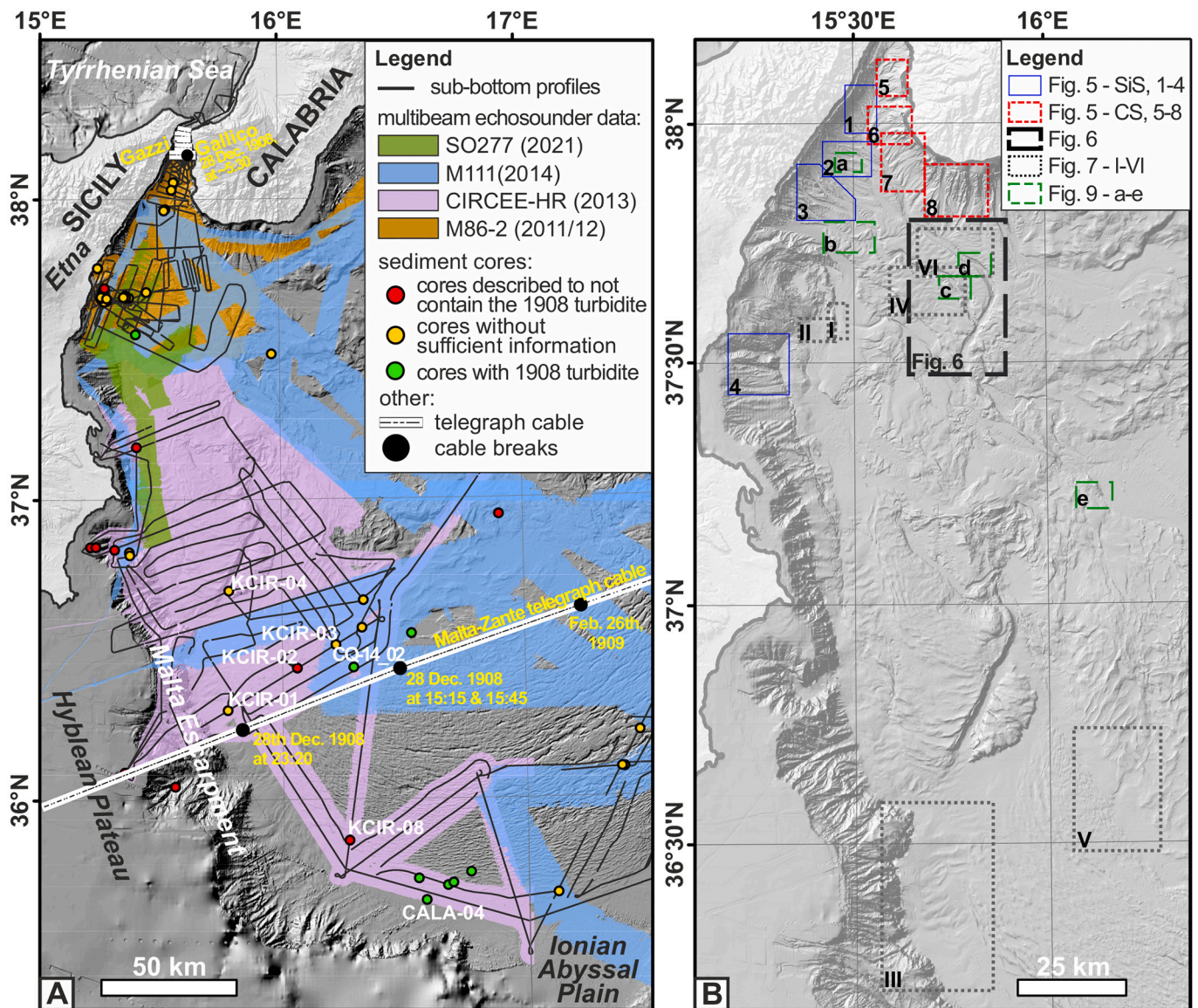

Fig. 2. A) Various data sets acquired across the western Ionian Basin used in this study consisting of multibeam echosounder data, sub-bottom profiles and sediment cores with the background bathymetry (grey shaded relief) from Gutscher et al. (2017). Important landmarks and the location of telegraph cables in 1908 are shown. B) Overview map showing the location of examples shown in other figures as highlighted by the different coloured and outlined boxes.

Here we hypothesise that the main passageway of the 1908 gravity flow was not directly connected to Mt. Etna. The previous attempts to reconstruct the 1908 gravity flow and older events were either based on low resolution bathymetry or sub-bottom and sediment core data with sparse coverage (Ryan and Heezen, 1965; Polonia et al., 2013, 2017; San San Pedro, 2016). There are large variations for proposed passageways and none of the studies identified any erosive or depositional bedforms along these passageways to support their findings (Fig. 1B). Thus, despite being one of the few known historic large run-out events, knowledge gaps regarding the source region, flow evolution and direction, and the type and scale of the erosional and depositional processes remain.

The aim of this study is to improve the current understanding about the 1908 gravity flow by inferring the: 1) potential passageways; 2) erosional and depositional bedforms along channel floors; 3) flow thickness; 4) flow velocity; and 5) potential source areas. Multiple data sets acquired over the past decade, consisting of multibeam echosounder data, sub-bottom profiles and sediment cores, have been used to address these objectives. Here we have one of the few known large run-out gravity flows associated with one of the biggest earthquakes (M_w 7.1) known to have affected the Central Mediterranean Sea (e.g., Tinti and Armigliato, 2003; Polonia et al., 2013; Gutscher et al., 2016, 2017). The absence of large-scale earthquake events ($M_w > 6$) in this region since 1908 (Rovida et al., 2022) implies that erosional and depositional features associated with the 1908 gravity flow are likely still preserved and have not been altered significantly by younger gravity flows. The largest earthquake in the study area since 1908 was the 1990 M_L 5.4 earthquake, offshore Augusta (Amato et al., 1995), which is not associated with any known tsunami or submarine landslides. The western Ionian Basin is, therefore, an ideal study site to improve our current understanding about large run-out events, especially as it is also one of the few events where information about cable breaks is available. The new findings can further be used for tsunami modelling to understand the potential involvement of gravity flows in tsunami generation. Better understanding of this gravity flow will have implications for similar events worldwide, and for better assessing marine geohazards offshore eastern Sicily.

2. Regional setting

Our study area comprises a part of the western Ionian Basin, from the Messina Straits down to the former location of the Malta-Zante telegraph cable, and from the Malta Escarpment to the location of the 4th cable break (Fig. 1A-B). The western Ionian Basin is a ~ 120 km-wide and ~ 280 km-long basin located in the central Mediterranean Sea south of Italy. It extends from the Messina Straits between Calabria and Sicily down to the IAP (Fig. 1A-B). The entire region is strongly affected by the Europe-African plate convergence, with the western Ionian Basin being part of the south-eastward trending Calabrian subduction zone (Anzidei et al., 1997; Goes et al., 2004; Barreca et al., 2021). This subduction zone is characterised by a complex tectonic regime in the form of coexisting compressional, extensional and uplifting deformation. As a consequence, the geomorphology of this region is strongly affected by the tectonic deformation, as apparent through differences in the accretionary wedge (Goes et al., 2004; Gutscher et al., 2017; Camerlenghi et al., 2020). The external, evaporitic wedge contains anticlines with confined sedimentary basins as a consequence of compression and Messinian salt deformation, while the more rigid internal, clastic wedge shows a mottled morphology with numerous submarine channels and basins (Fig. 1A) (Polonia et al., 2011; Gutscher et al., 2017). The internal and external CAW is separated by an up to 1 km-high escarpment, otherwise known as "the wall" (Fig. 1B) (Gutscher et al., 2017). The Alfeo Seamount (AS) and the westernmost lobe (W-lobe) of the CAW are noticeable features, as they appear as separated morphological structures within this tectonic setting (Fig. 1A-B) (e.g., Gutscher et al., 2017). The Messina Straits comprise the northernmost part of the western

Ionian Basin and is generally considered to be a northeast-southwest trending graben structure extending between north-eastern Sicily and southern Calabria (Fig. 1A) (Valensise and Pantosti, 1992). This extensional component is accompanied by regional uplift of the adjacent continental margins of northern Sicily (Peloritani Massif) and southern Calabria (Aspromonte Massif), as evident through the occurrence of marine terraces along the mainland up to 1300 m above sea level (Valensise and Pantosti, 1992). The uplift occurs at rates of 0.9 to 1.4 mm yr^{-1} and can be dated back to ~1 Ma BP (Valensise and Pantosti, 1992). This ongoing uplift results in large onshore erosion and consequent high sediment discharge into onshore river systems (Goswami et al., 2014; Ridente et al., 2014). The presence of narrow (<1 km-wide) continental shelves allow these onshore river systems to almost directly discharge sediment into the canyon heads (Goswami et al., 2014, 2017; Ridente et al., 2014). Sedimentation within the western Ionian Basin is further influenced by bottom currents (Sparnocchia et al., 2011; Micallef et al., 2016; Rebesco et al., 2021). Sediment waves at the foot of the Malta Escarpment are interpreted as a direct result of these currents (Rebesco et al., 2021). Measurements at localised mooring stations in this area showed a predominant south-south-westward directed bottom water flow with current velocities of >10 cm s^{-1} (Rebesco et al., 2021).

The entire region is prone to earthquakes, many of which are associated with tsunamis (e.g., 1169, 1693, 1908) and sediment gravity flows, that over the past few centuries caused significant fatalities and infrastructural damage (Omori, 1909; Ryan and Heezen, 1965; Anzidei et al., 1997; Tinti and Armigliato, 2003; Polonia et al., 2013). The sources of many of these events are still debated (e.g., Tinti and Armigliato, 2003; Billi et al., 2008; Argnani et al., 2009b). Barreca et al. (2021) just recently proposed the 1908 M_w 7.1 causative earthquake fault to be located within the Messina Straits and the northern portion of southern Calabria considering the distribution of the marine terraces. Different scenarios have also been proposed and tested to explain tsunami generation in this region. Simulations on the 1908 tsunami, for example, considered a submarine landslide in addition to the earthquake source. Most successful simulations considered landslides offshore Nizza (Favalli et al., 2009) or Fiumefreddo (Billi et al., 2008) of eastern Sicily and multiple smaller failures along the southern Calabria continental slope (Schambach et al., 2020) (Fig. 1B). A submarine landslide would also be a likely source for the formation of the 1908 sediment gravity flow, but a large sediment mass failure has not been identified in these regions (Argnani et al., 2009b; Gross et al., 2014). Many of the proposed landslide locations were based on morphological observations without confirmation by dating and sub-bottom or high-resolution seismic reflection data.

3. Methods

3.1. Multibeam echosounder

The multibeam echosounder data were acquired during research expeditions M86–2 (2011/12), CIRCEE-HR (2013), M111 (2014) and SO277 (2020) using the Kongsberg Simrad EM122 (M86–2, M111, SO277) and EM302 (CIRCEE-HR) (Fig. 2A). These systems are operated at nominal frequencies of 12 kHz (EM122) and 30 kHz (EM302). The available data cover the upper and mid-slope area of the western Ionian Basin (~28,000 km^2) (Fig. 1-3). The data were processed using the open-source software MB-system. Data were gridded at 30 m resolution for regions with <3000 m water depth (mwd) and at 50 m resolution for regions with >3000 mwd. Backscatter data were extracted from the multibeam swath bathymetry data acquired using the primary deep-water systems and processed using the MB-back-angle and MB-grid function of MB-system (Manik et al., 2015). The backscatter data were gridded at the same resolution as the multibeam bathymetry. The data were supplemented by the bathymetric compilation of Gutscher et al. (2017). The Gutscher et al. (2017) bathymetric map is gridded at 50 m and covers the entire western Ionian Basin (~36.000 km^2) (Figs. 1, 2A).
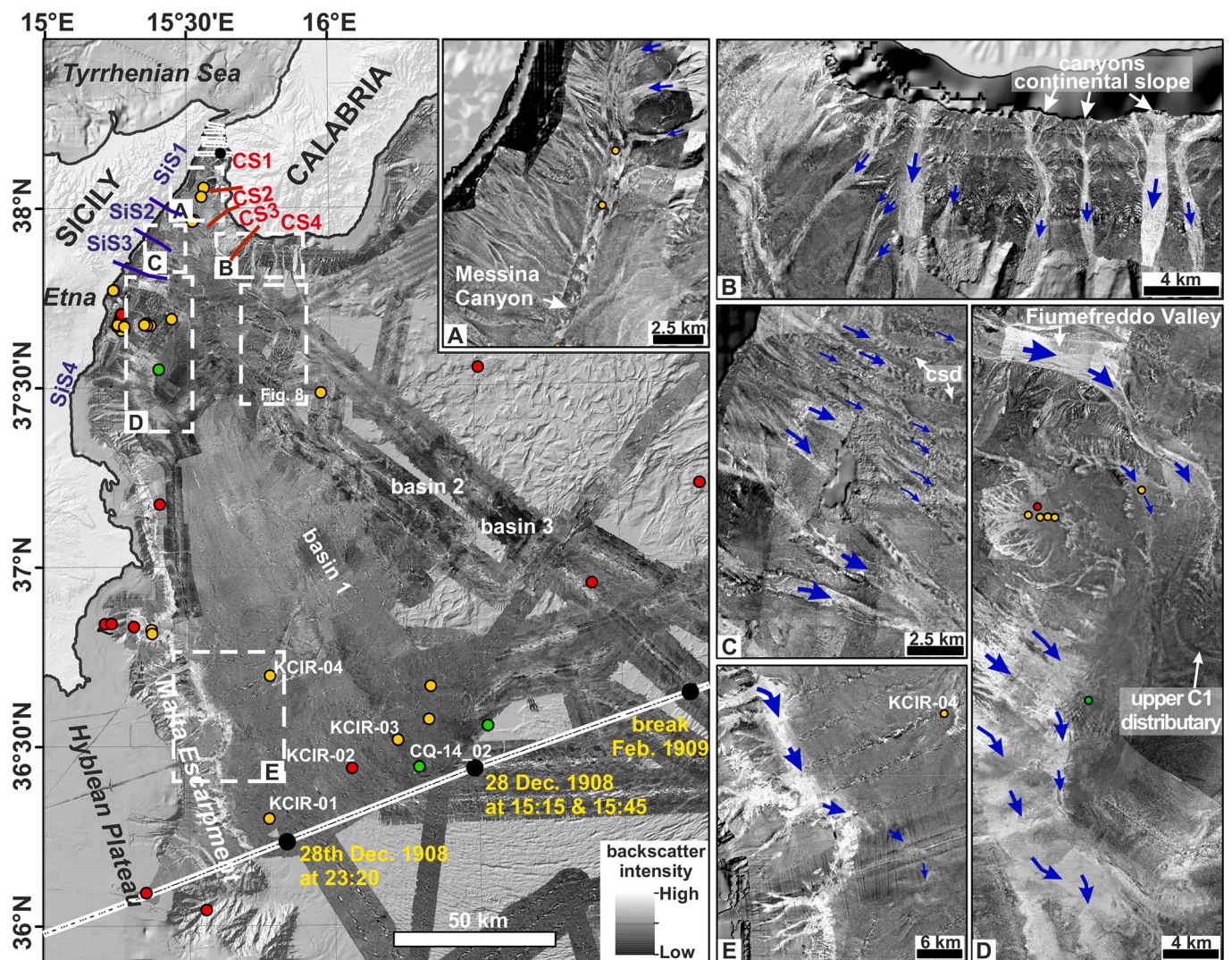
Fig. 3. Backscatter data covering the western Ionian Basin with locations of telegraph cables (white dotted lines), cable breaks (black dots) and sediment cores. Green dots represent cores with confirmed 1908 turbidite, yellow dots are sediment cores without sufficient information, red dots are described to not contain the 1908 turbidite. Labelled sediment cores are discussed in this study. Labelled blue and red lines along Sicily (SiS1 to SiS3) and Calabria (CS1 to CS4) indicate different zones of canyon systems. White dotted boxes (A-E) are locations of zoomed sections shown to the right. Blue arrows indicate the distribution and interpreted direction of flows with different sizes according to backscatter intensity. (For interpretation of the references to colour in this figure legend, the reader is referred to the web version of this article.)

Specifications on the acquisition are available in e.g., Krastel et al. (2014), Gutscher et al. (2013), and Urlaub et al. (2022).

Multibeam bathymetry and backscatter data were used to characterise the morphology of the western Ionian Basin and to define different conduit systems and source areas for the 1908 gravity flow (Fig. 4). ArcMap was used to map geomorphological features such as the channel floor and thalweg, basins, interchannel heights, escarpments and bedforms. Backscatter data, which are a measure of the reflectivity of a surface, are representative of surface roughness, slope gradient, and sediment grain size (Augustin et al., 1996) (Fig. 3).

3.2. 2D sub-bottom profiles

Sub-bottom data were acquired during research expeditions M86–2 (2011/12) and CIRCEE-HR leg 1 and leg 2 (2013) using Chirp and Atlas Parasound P70 acquisition systems (Fig. 2A). The Chirp data were acquired using a signal frequency bandwidth of 1.8 to 5.3 kHz (Gutscher et al., 2013). This system images the upper 50 to 80 m of the sub-bottom with a minimum horizontal resolution of 11 to 20 m in 1000 mwd and 20 to 40 m in 4000 mwd (Fresnel zone) (Gutscher et al., 2013). The

vertical resolution of this system is ~0.75 m (San Pedro et al., 2017). The Parasound system is a parametric echo sounder operating at 4 kHz; the system allows imaging of the upper 100 m of the sub-bottom at a vertical resolution of 0.15 m (Teledyne Marine, 2017). These parametric echo sounders have a narrow opening angle of 4.5°, which allows data acquisition with fewer side-echoes when compared to conventional systems (e.g., boomer, chirp) (Teledyne Marine, 2017). The minimum horizontal resolution is 70 to 280 m between 1000 and 4000 mwd (Spieß, 1993). Detailed information about specifications of the systems used are available in the cruise reports (e.g., Krastel et al., 2014; Gutscher et al., 2013). Sub-bottom profiler data were used to map the distribution and relationships of acoustic facies (e.g., high/low amplitude sub-bottom echoes, onlapping) according to Damuth (1975, 1980) and Damuth and Olson (2015). This information was used to infer sediment grain size, erosion, and long-term deposition in order to reconstruct erosional and depositional processes along the upper sediment strata as a consequence of recent gravity flow activity. A map showing the acoustic facies distribution was generated. We attempted to interpolate facies between adjacent profiles if the spacing between the sub-bottom profiles was not too large (<10 km) and where acoustic
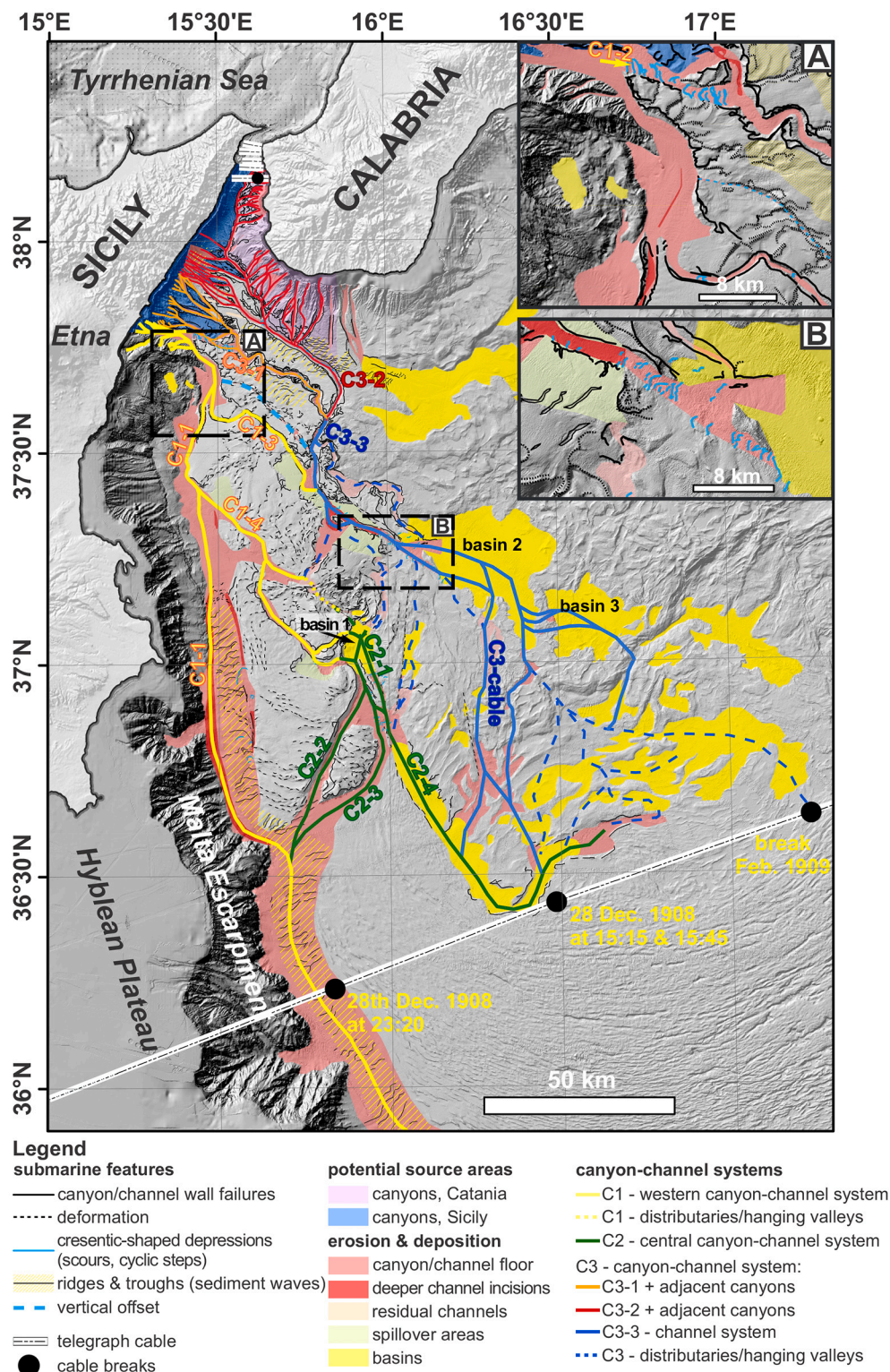
Fig. 4. Shaded multibeam bathymetry relief with geomorphic interpretation showing the distribution of channel floors, basins and various erosional and depositional bed-forms. Coloured lines (yellow, green, orange, red and blue) show mapped canyons and channels. Note that blue lines represent a continuation of red and orange. This geomorphological map of the western Ionian Basin was generated by integrating information from the various data sets and results from Gutscher et al. (2016, 2017), Polonia et al. (2013, 2017) and San San Pedro, 2016. (For interpretation of the references to colour in this figure legend, the reader is referred to the web version of this article.)

facies were associated with specific morphological features (e.g., sediment waves, basins, steep slopes). IHS Kingdom Suite™ was used for the data analysis of the sub-bottom data. A sound velocity of 1500 ms^{-1} was used to convert from two-way travel time into metres.

3.3. Sediment cores

Sediment gravity cores were collected from the mid- to south western Ionian Basin during research expedition CIRCEE-HR (Figs. 2A, 3, Table 1) (Gutscher et al., 2013). The sediment cores were visually described in the laboratories of the European Institute for Marine Studies at the University of Brest (IUEM, France). The visual core description included a re-assessment of sediment lithology, sediment structures, stiffness and colour. Oher core analysis (e.g., density, grain size, age) carried out by and published in San San Pedro, 2016 and San Pedro et al. (2017) were considered in this study. The information was

Table 1
List of CIRCEE-HR sediment cores used in this study.

Core ID	Cruise (year)	Latitude	Longitude	Core length (m)
KCIR-01	CIRCEE-HR (2014)	36.297	15.775	3.6
KCIR-02	CIRCEE-HR (2014)	36.437	16.062	5.1
KCIR-03	CIRCEE-HR (2014)	36.514	16.221	3.94
KCIR-04	CIRCEE-HR (2014)	36.695	15.782	6.38
KCIR-08	CIRCEE-HR (2014)	35.862	16.269	7.37

used to ground truth findings in the sub-bottom data and to reconstruct the depositional behaviour of the 1908 gravity flow.

4. Results

The western Ionian Basin is characterised by numerous, deeply incised (~100 m-deep) channel systems. Three main passageways for gravity flows, the western, central and eastern canyon-channel systems (**C1, C2, C3**), were distinguished based on their morphological characteristics (e.g., extension, continuity) (Fig. 4). In this study, the term "canyon" refers to conduits along the continental slopes as defined by Amblas et al. (2018). Goswami et al. (2014) previously distinguished different canyon systems for the continental slope adjacent to the Messina Straits. Here we modified this previous classification and expanded it southward of the Messina Straits (Fig. 3). The term "channel" refers to conduits extending beyond the base of the continental slope. The term "canyon-channel systems" refers to continuous systems of canyons, channels and adjacent distributaries. The term acoustic facies or facies is used to describe observations from sub-bottom profiles, while sedimentary features are described as sediment sequences with units.

4.1. Morphology

4.1.1. Canyons

4.1.1.1. Sicily and Malta Escarpment.
The eastern Sicilian continental slope (7°) and Malta Escarpment (~11°) show various canyons that have second and third order tributaries (Fig. 5). The canyons generally widen from 250 to 2100 m towards Mt. Etna, but are narrower (500–1000 m-wide) with less tributaries along the Malta Escarpment (Figs. 1; 3A, 3C). The largest canyon system within the research area is Fiumefreddo Valley, offshore Fiumefreddo (2.5 km-wide, ~150 m-deep) (Fig. 3D). Differences in the geomorphology and backscatter intensities allow us to distinguish four zones of canyon systems along the eastern Sicilian margin; termed **SiS1** to **SiS4** (Figs. 3, 5). Individual canyons are easily recognizable within all zones except **SiS1**, which shows a high density of shallow, ~30 m-deep canyons. High to moderate backscatter patches are present, but generally confined to the canyon floor, while the background morphology shows low to moderate backscatter patches (Figs. 3A, C, D).

4.1.1.2. Southern Calabria.
Canyon systems of the southern Calabrian slope (6–8°) can be distinguished into four zones, termed **CS1** to **CS4** (Figs. 3, 5). There are fewer, but generally broader (~800 m-wide) canyons along the Calabrian slope in comparison to the opposite eastern Sicilian slope (Figs. 3A-B). Canyons in all four zones show similar incision depths (50–100 m-deep) and often have second and third order tributaries (Fig. 5). **CS1** and **CS4** show high backscatter patches along canyon floors (Fig. 5). **CS2** and **CS3** show moderate to high backscatter patches along the entire slope, which makes it difficult to distinguish single canyons from the background morphology on the basis of backscatter data alone (Figs. 3A-B, 5).

4.1.2. Western canyon-channel system
The **western canyon-channel system (C1)** consists of four subsystems (Fig. 4). The main system (**C1–1**) extends from Fiumefreddo

Valley north of Mt. Etna down to the IAP with the seafloor gradient decreasing from 0.8 to <0.1° (Figs. 4, 4A, 6). It leads directly to the third break recorded along the Malta-Zante telegraph cable, which is located ~200 km south of Fiumefreddo Valley (Figs. 4, 6). The main channel extends parallel to the eastern Sicilian margin and the Malta Escarpment (Fig. 4). Tributaries into **C1–1** are exclusively from **SiS4** (Fig. 3). The channel floor is ~3 km-wide in the vicinity of Mt. Etna and up to ~15 km-wide towards the IAP, with an average incision depth of ~150 m (Fig. 4A). Large-scale, straight to sinuous shaped ridges and troughs (~500 m-wide, ~25 m-high) are apparent perpendicular to the channel floor along the southern portion of **C1–1** (37° 06′ N - 35° 46′N) (Figs. 4, 7). **C1–1** has three east- to southeastward-oriented distributary channels (Fig. 4). The upper two distributaries (**C1–2** & **C1–3**) merge into **C3** (Fig. 4). The southern distributary (**C1–4**, 300–500 m-wide, ~150 m-deep) bifurcates into second order distributaries, which merge into **C2** (Fig. 4). **C1** is mostly characterised by low backscatter intensities (Fig. 3). Exceptions are higher backscatter patches in vicinity to **SiS4** canyons, but the backscatter intensity diminishes <25 km downslope from the confluences (Figs. 3C-E).

4.1.3. Central canyon-channel system
The **central canyon-channel system (C2)** is located in the middle to southern part of the western Ionian Basin and consist of four subsystems. There is no direct connection to canyon systems of the continental slopes, but both **C1–4** and **C3** merge into **C2–1** through up to 500 m-wide distributary channels (Figs. 4, 6). **C2–1** consists of a steep (~3°) basin complex with several depressions and 180 to 300 m-high knickpoints leading into **basin 1** (~112 km^2) (Figs. 4, 6). South of **basin 1,** **C2–1** bifurcates into three branches, **C2–2, C2–3** and **C2–4** (Fig. 4). Zones of positive relief (up to 80 m-high) are evident along the seafloor of **basin 1,** the bifurcation zone, **C2–2** and **C2–3** (Figs. 4, 6). **C2–2** and **C2–3 (**2–4 km-wide, 400–500 m-deep) encompass Alfeo Seamount and confluence into **C1–1** (Fig. 4). Slope gradients of <0.1° are observed along up to 15 km-long sections of both systems. **C2–4** is a southward extending, up to 6 km-wide and ~ 100 m-deep elongated basin between the external and internal CAW (Fig. 4). Slope gradients are <0.1° over a distance of up to 60 km (Figs. 4, 6). A ~ 20 m-high vertical offset is observed along the middle section of **C2–4,** which is related to a linear feature that is oriented almost perpendicular to the basin. Towards the first two cable breaks **C2–4** confluences with **C3** distributaries (Fig. 4). **Basin 1** and **C2–4** show low backscatter patches, while **C2–2** and **C2–3** show low to moderate backscatter patches (Fig. 3).

4.1.4. Eastern canyon-channel system
The **eastern canyon-channel system (C3)** extends from the northern part of the Messina Straits down to the external CAW and leads directly to the first two cable breaks of the Malta-Zante telegraph cable (Figs. 4, 6). Tributaries into **C3** are almost exclusively from northeastern Sicily (**SiS1 to SiS3**) and Southern Calabria (**CS1 to CS4**). **C3** is divided into three sub-systems, each showing an abundance of characteristic bedforms (Figs. 4, 8A-C). Numerous localised scarps are evident along channel walls especially along the upper part of **C3** (Fig. 8).

The western sub-system (**C3–1)** is strongly meandering, 150 m-deep and up to 2 km-wide (Fig. 4). Low to moderate backscatter patches dominate the channel floor, while high backscatter patches are abundant along the steep (~18°) channel walls (Fig. 8B). **C3–1** has tributaries from **SiS3** and from Fiumefreddo Valley via **C1–2** (**SiS4**) (Figs. 3C, 4A). Large-scale (~25 m-deep, up to 1.9 km-long) crescent-shaped depressions are evident along the seafloor downslope of the confluence with **C1–2** (Figs. 4A, 9). 2D geomorphological profiles from this type of bedforms show that they have a steep lee and flat stoss side (Fig. 9). Localised, small- to medium-scale (~20 m-deep, 200–300 m-long) crescent-shaped depressions are further observed along the lower part of **C3–1** (Figs. 8A, C, 9). The interchannel height between **C1** and **C3–1** shows irregular, crescent-shaped ridges and troughs (20–30 m-high,
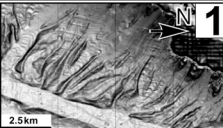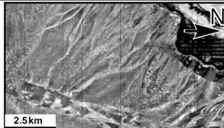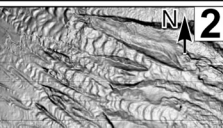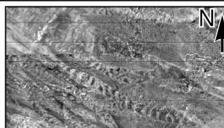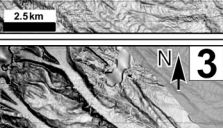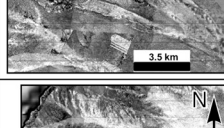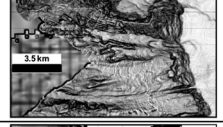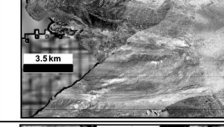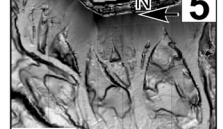
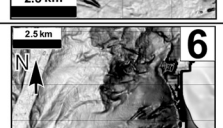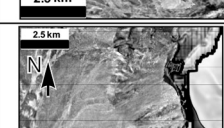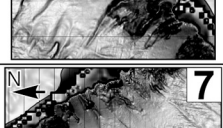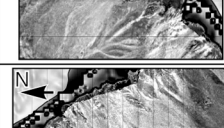| System	Geomorphological characteristics	Backscatter	example bathymetry	example backscatter
SiS1 Messina - Nizza di Sicilia	300-400 m-wide/30 m-deep single canyons	**High** - canyon floor **Moderate** - background morphology		
SiS2 Nizza di Sicilia - Sant' Alessio Siculo	2nd/3rd order tributaries up to 4.5 km-wide/100 m-deep; crescentic-shaped bedforms along canyon floors (10-25 m-high, 200-400 m-long)	**Moderate/High** - canyon floor **Moderate/Low** - background morphology		
SiS3 Sant' Alessio Siculo - Naxos	~900 m-wide/up to 100 m-deep 2nd order tributary canyons; crescentic-shaped bedforms more scattered compared to SiS2	**High** - canyon floor **Low/Moderate** - background morphology		
SiS4 Naxos & Malta Escarpment	mainly single canyons	**High** - canyon floor **Low/Moderate** - background morphology		
CS1 Concessa – San Leo	~800 m-wide/~50 m-deep canyons with 1st/2nd order tributaries	**High** - canyon floor **Low/Moderate** - continental slope		
CS2 San Leo – Bocale	Single canyons cannot be distinguished from background morphology	**Moderate/High** - canyon floor & continental slope		
CS3 Bocale – Saline Joniche	Individual channels along the upper margin merge into 2nd order ~800 m-wide/50 m-deep tributary canyons	**High** - canyon floor & continental slope		
CS4 Saline Joniche – Marina di San Lorenzo	Gullies along the upper slope lead into up to 1 km-wide/~100 m-deep, single canyons	**High** - canyon floor **Low** - background morphology		

Fig. 5. Canyon systems along the Sicilian and Calabrian continental slope divided into different zones according to geomorphological characteristics and backscatter intensities. Examples representative of the characteristics of each system are shown to the right. See Fig. 2B for location of examples (1–8). Note that backscatter examples, to the right of the bathymetry examples, image the same location.

1–1.25 km-long) (Figs. 7, 8A, C).

The eastern channel **(C3–2)** originates from the Messina Sill, which connects the Tyrrhenian Sea and western Ionian Basin (Fig. 4). Tributaries are from **SiS1, SiS2** and **CS1 to CS4** (Figs. 3, 8). The thalweg of **C3–2** (210 m-deep, up to 1.7 km-wide) is straight, except for two ~90°-steep bends (Figs. 1, 3, 4). Trains of large-scale crescent-shaped depressions (~25 m-deep, 1–3.9 km-long) are observed along the second bend (Figs. 6, 8A, C, 9). Both, the steep channel walls (~16°) and the

channel floor, show high backscatter patches (Fig. 8B). The trimline or upper limit of high backscatter intensities is at ~170 m from the channel floor. The lower portion of the Calabrian slope and inter-channel height adjacent to C3–2 show perpendicular to sub-parallel oriented straight to sinuous shaped ridges and troughs (~20 m-high, ~1 km-long) (Figs. 7, 8A, C). There is a higher abundance and regularity of those bedforms adjacent to C3–2 than C3–1 (Fig. 8).

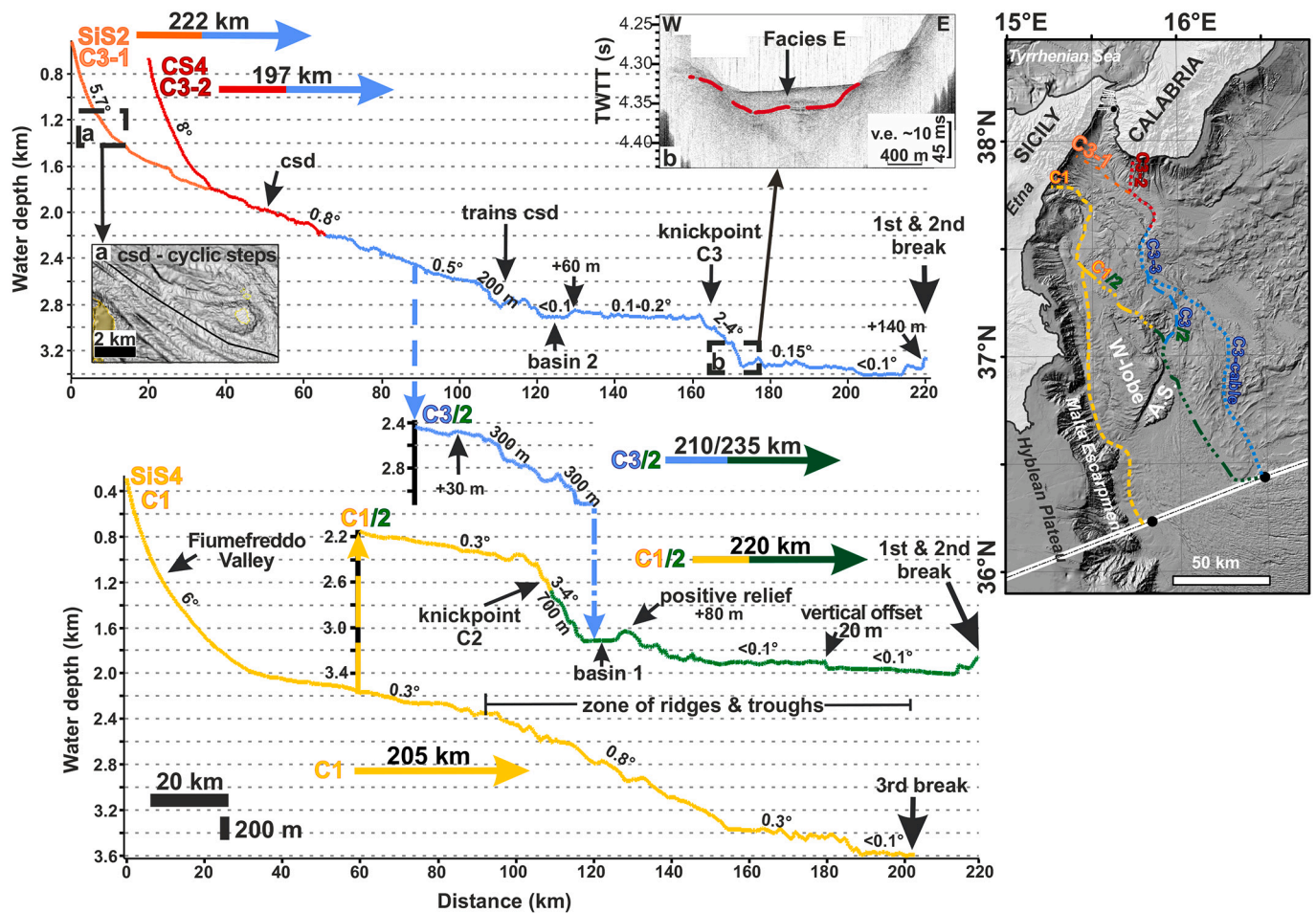**C3–1** and **C3–2** merge into **C3–3**, which is a southward extending

Fig. 6. Geomorphological profiles starting from different source regions (e.g., SiS2) that follow the identified canyon-channel systems (**C1, C2, C3**) downslope to breaks recorded along the Malta-Zante telegraph cable in 1908. The distance from different potential source areas to the cable breaks are provided along the coloured horizontal arrows. Geomorphological features and changes in the slope gradients are highlighted. Coloured vertical dotted arrows show confluences to other profiles. Inlet (a) shows the trains of crescentic-shaped depression (csd) within canyons of **SiS2** and (b) shows acoustic Facies E below **C3**-knickpoint (see section 4.2). The dotted red line in (b) highlights the lower boundary of Facies E. For profile locations see dotted lines with system names (e.g., **C1**) shown in the map to the right. (For interpretation of the references to colour in this figure legend, the reader is referred to the web version of this article.)

channel system with numerous distributaries (Fig. 4). The majority of channels follow linear features leading in and out of two large and flat (<0.1°) basins (**basin 2**, 624 km^2 & **basin 3**, 324 km^2) (Fig. 4). A well-developed train of large-scale crescent-shaped depressions (up to 50 m-deep, 500–1000 m-long) is evident for 18 km along the channel floor leading into **basin 2** (Figs. 4B, 9). Almost all distributaries of **C3–3** are hanging valleys with elevation differences of 30 to 70 m to the main channel (Fig. 6). Slope gradients of <0.2° are observed along up to 40 km-long sections of these channels (Fig. 6). One of the hanging valleys (**C3-cable**) extends from **basin 2** towards the cable breaks (Fig. 4). It crosses a 200 m-high knickpoint that is part of the escarpment separating the external and internal CAW (Figs. 1, 6). Downslope of the knickpoint this distributary bifurcates into a western and southern branch (Fig. 4). The southern branch leads directly to the cable breaks, while the western branch leads into **C2–4** (Fig. 4). The distance from **CS4** and **SiS2** to the cable break location via this southern branch is ~199 and 222 km respectively (Figs. 4, 6). High backscatter patches are evident along tributaries, channel floor and walls down to **basin 2**, especially within **C3–2** (Figs. 3, 3C, 8B). **Basin 2** and **basin 3** are dominated by low backscatter signals with localised patches of high backscatter intensity along routes leading towards distributary channels (Fig. 3).

4.2. Sub-seafloor acoustic facies distribution and relationships

Six main sub-seafloor acoustic facies are distinguished and mapped across the study area following the classification scheme provided by Damuth (1975, 1980) and Damuth and Olson (2015) (Figs. 10-12, 13). The facies are distributed as follows:

1. **Facies A** is characterised by indistinct, sharp, prolonged bottom echoes with no sub-bottom reflections. It characterises sections of canyon and channel floors and is most abundant within the Messina Straits (Figs. 12, 13A).

2. **Facies B** is characterised by indistinct, hyperbolic bottom echoes with varying vertex elevations and no sub-bottom reflections. It occurs throughout the research area (Fig. 13A-B). **Facies B-1** (small to medium, regular overlapping hyperbolic bottom echoes) is abundant along channel floors, especially within the northern part of the research area (**C1–1, C1–2, C3–1, C3–2**) (Figs. 10, 12, 13A). **Facies B-2** (medium to large, irregular overlapping hyperbola) is common along steep slopes of channel walls and morphological heights (e.g., Malta Escarpment, Alfeo Seamount, the Western Lobe) (Figs. 10, 12, 13A-B).

3. **Facies C** is characterised by indistinct, semi-prolonged bottom echoes with intermittent sub-bottom echoes. It often occurs next to **Facies E**. **Facies C** is abundant along channel floors within the
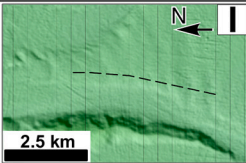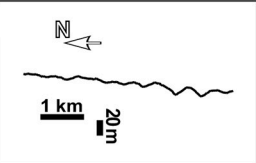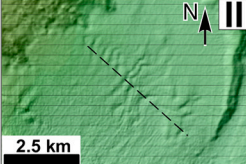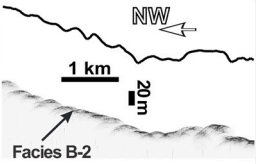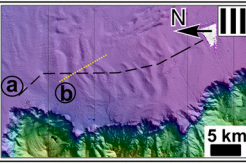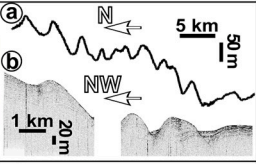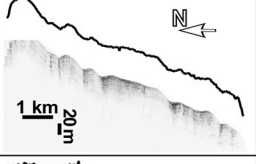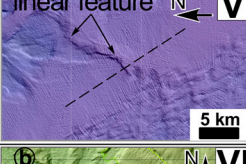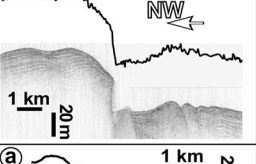
Ridges and troughs - bedforms of overall positive relief

System	Location	Bedform description	Height (m)	Wavelength (m)	Distance (km)	Morphological examples	morphological or seismic profile
C1	Interchannel height between C1 and C1-3	Regular, straight to sinuous shaped, perpendicular to channels	4-10 m	500-700 m	6 km	I — 2.5 km	1 km / 20 m
C1	Lower slope proximal to Mt. Etna	Closely spaced, regular, straight to sinuous shaped sections, channel parallel	6-13 m	500-700 m	3-4 km	II — 2.5 km	NW 1 km / 20 m — Facies B-2
C1	Lower part of C1-1; parallel to Malta Escarpment	Closely spaced, regular, sinuous shaped sections; perpendicular to the channel floor	20-30 m	1500-3000 m	150 km	III — 5 km	(a) NW 5 km / 50 m; (b) NW 1 km / 20 m
C1 - C3 (C3-1)	Interchannel height between C1 & C3-1	Irregular, crescent- to sinuous shaped; channel parallel	20-30 m	1000-1250 m	14 km	IV — 5 km	N 1 km / 20 m
C2-4	channel floor elongated basin	almost plane, lightly crescentic-shaped, nearly oblique to channel	1.5-4.5 m	500-600 m	10 km	linear feature V — 5 km	NW 1 km / 20 m
C3 (C3-2)	Calabrian slope adjacent C3-2	Closely spaced, regular, straight to sinuous shaped; oblique to the channel	10-20 m	550-1000 m	11 km	VI — 5 km	(a) NW 1 km / 20 m
C3 (C3-1- C3-2)	Interchannel height between C3-1 & C3-2		15-30 m	1000-1250 m	15 km		(b) N 1 km / 20 m

Fig. 7. Location and characteristics of ridges and troughs found within different conduit systems of the western Ionian Basin. Images to the right show morphological examples, sub-bottom profiles (where available) and 2D geomorphological profiles for each bedform. For location of each example (I-VI) see Fig. 2B, and for the location of profiles see dashed lines on the morphological image to the left.

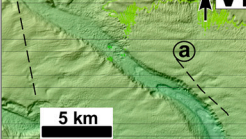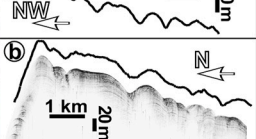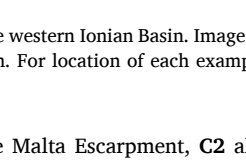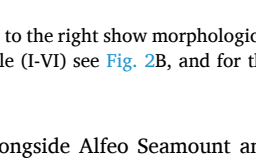middle and southern part of the research area, especially **C1** and the upper part of **C2** (Figs. 10, 11, 13B). Along **C1** it is apparent along crests of **Facies F** (Figs. 10, 13B).

4. **Facies D** characterises distinct, sharp bottom echoes with continuous at times intermittent parallel sub-bottom reflection. This facies is abundant throughout the research area (Fig. 13A-B). It is found along canyon levees of **SiS2** and **CS1** and interchannel heights (Figs. 12, 13A). **Facies D** dominates the middle and southern part of the research area, especially **C2–4** (Figs. 11, 13B). The external CAW shows a mixture of **Facies D** and **Facies B2** echo characteristics (Fig. 13B). **Facies D** reflections often onlap deeper reflections resulting in thinning of reflection packages towards the sides of basins and on top of adjacent morphological heights, which is especially noticeable within **C2–4** (Fig. 11).

5. **Facies E** describes the topmost reflection unit characterised by lenses and layers of indistinct bottom echoes with transparent or incoherent, internal reflections. It is found at the foot of continental slopes and canyon walls and is observed adjacent to **Facies C** along the channel floor of **C1–1** within troughs of **Facies F** (Figs. 10, 13A-B). Layers and lenses of **Facies E** are generally <7.5 m-thick (Figs. 10-12). They are locally up to 20 m-thick such as along **C1–1**

towards the Malta Escarpment, **C2** alongside Alfeo Seamount and downslope the ~200 m-high **C3–3** knickpoint (Figs. 10-12). From **C2–2** and **C2–3** towards **C2–4,** **Facies E** becomes covered by stratified reflections of **Facies C** and **D** (Fig. 11). An up to 10 m-thick layer of **Facies E** is evident along the middle to lower continental slope of **CS2** (Fig. 12).

6. **Facies F** is characterised by distinct to indistinct sharp bottom echoes with parallel to sub-parallel sub-bottom reflections that appear wavy through apparent downslope truncating and onlapping reflections. It is observed along interchannel heights between **C1** and **C3,** where **Facies F** is tilted and thickens towards **C3–2** (Figs. 12, 13A-B). **Facies F** is further evident along the southern portion of **C1–1** and **C2–4** (Fig. 13B). This facies is tilted up-slope and appears symmetric along **C1–1**, but shows progressive downslope thinning and a decrease in dimension across a 20 m-high vertical offset present along **C2–4** (Figs. 7, 14).

4.3. Sedimentological characteristics

CIRCEE-HR sediment cores show sequences of stacked, different coloured sediment units (Figs. 2A, 3, 10). KCIR-04 collected from the
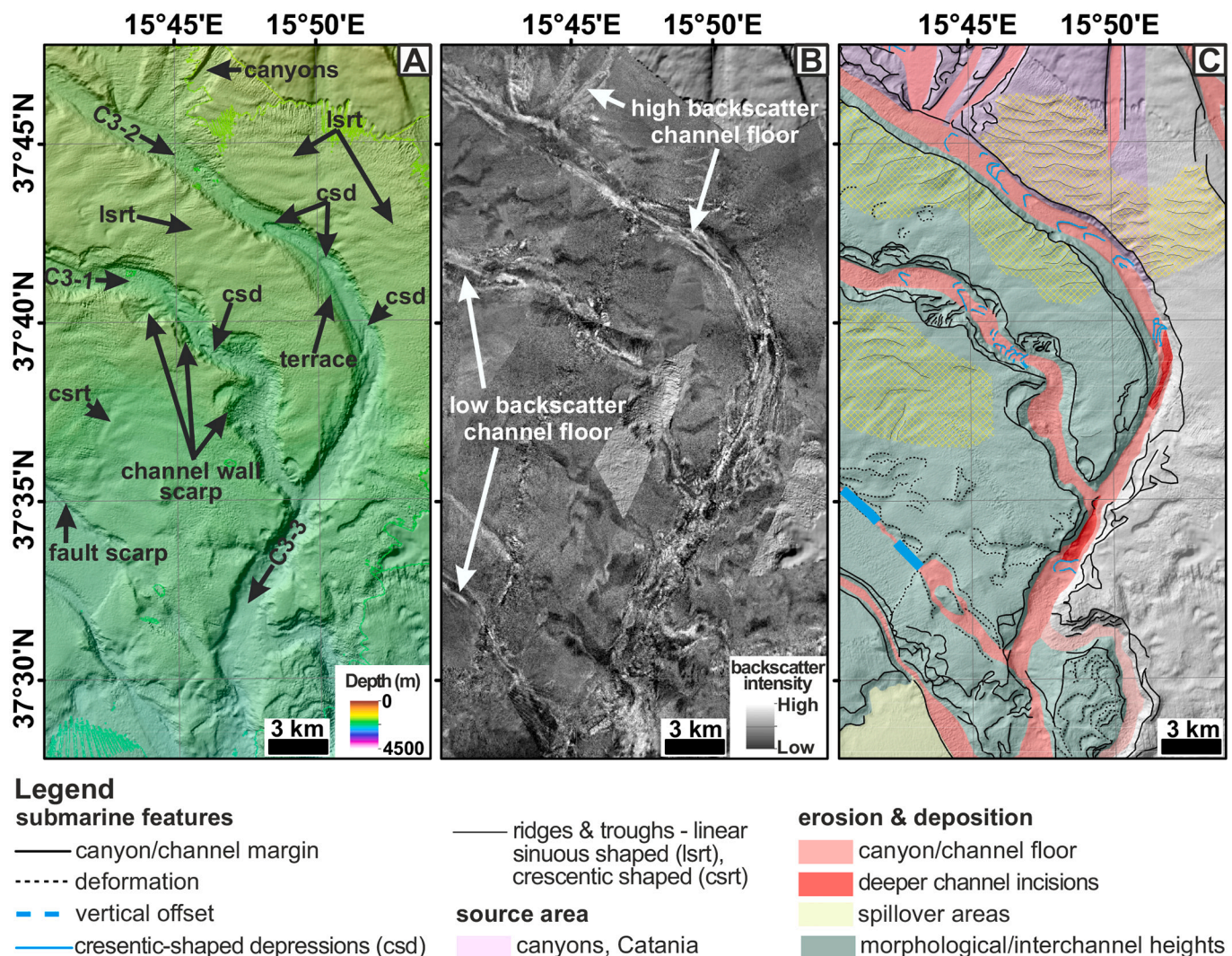
Fig. 8. Comparison of bathymetry (A), backscatter intensity (B) and interpreted morphologic regions (C) in the eastern Messina Straits (**C3**). (A & C) highlight the distribution of different geomorphological features, (B) shows the distribution of high backscatter patches and (C) the interpretation such as location of deeper thalweg incisions. For location within the research area see Figs. 2B and 3.

southern portion of **C2–2** towards **C1–1** shows six sequences of stacked sediment units within the upper 50 cm (Fig. 10). Each sequence is <10 cm-thick with a sandy base unit being <4 cm-thick. KCIR-01 collected along the channel floor of **C1–1** proximal to the third cable break shows a similar characteristic as KCIR-04 (Fig. 10). There are up to five sequences of stacked sediment units in the upper 50 cm (Fig. 10). In comparison, KCIR-08 that was collected further downslope of **C1–1** towards the IAP shows four >10 cm-thick sequences (Fig. 10). KCIR-03 was collected within the southern part of **C2–4** in proximity to CQ14_02 described in Polonia et al. (2017) (Figs. 2A, 11). There are three different coloured units in the upper 1.09 m (T1; Fig. 11). The base of T1(Unit 1, 41–109 cm) is a massive, dark grey medium to coarse sand with a high abundance of mica, which is overlain by a 41 cm-thick mud cap (0–41 cm) (Fig. 11). KCIR-02 was collected in proximity to KCIR-03 within a basin of the external CAW (Fig. 2A). The upper 40 cm contains three sequences of stacked sediment units with a 4 cm-thick unit of dark grey to black, stiff, fine sand at the top that resembles Unit 1 of KCIR-03 (Fig. 11).

5. Discussion

5.1. Geophysical and sedimentological indicators to reconstruct recent erosional and depositional processes

Facies A and B-1 along canyon and channel floors are associated with high backscatter patches and often but not necessarily with crescentic-shaped depressions (e.g., along **SiS2** canyon floors) (Figs. 3C, 9, 13A). **SiS2, SiS4, CS1** and **CS4** show the highest backscatter intensities along the continental slope (Figs. 3, 5). River systems discharge high amounts of sediment from onshore erosion and flash floods almost directly into the canyon heads of these systems (Goswami et al., 2014; Ridente et al., 2014). We interpret crescentic-shaped depressions such as those observed along **SiS2** and **C3** channel floors as scours (Fig. 9) (cf., Paull et al., 2014; Slootman and Cartigny, 2020). Scours are described to often contain coarser grained material (e.g., Hage et al., 2018). These net-erosional cyclic steps are observed along canyon and channel floors worldwide (e.g., Symons et al., 2016; Covault et al., 2014, 2017). They are widely interpreted as a result of erosion through bypassing turbidity currents as cyclic hydraulic jumps cause a shift from Froude supercritical to subcritical flow conditions (e.g., Fildani et al., 2006; Covault et al., 2014; Slootman and Cartigny, 2020). **Facies A** and **B-1** with high backscatter patches are, therefore, interpreted to represent either coarse
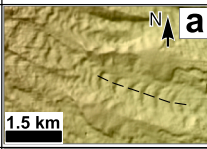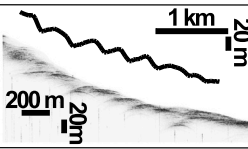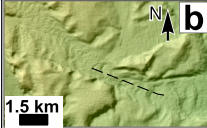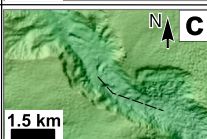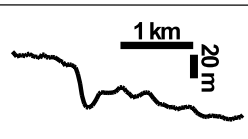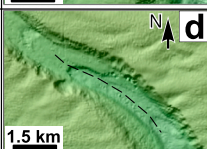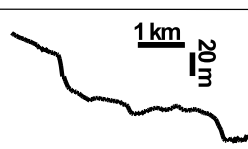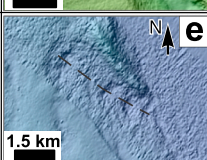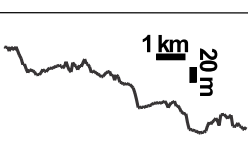
Depressions - bedforms with negative relief								
System	Location	Bedform description	Depth (m)	Wavelength (m)	Width (m)	Distance (km)	Morphological examples	morphological or seismic profile
C3 (SiS2)	Canyon floor, SiS2	Trains of large-scale crescentic-shaped depressions; channel parallel	10-25 m	200-500 m	400-500 m	8 km		
C3 (C3-1)	beneath the confluence with Fiumefreddo Valley (C1-2)	Train of large-scale crescentic-shaped depressions	~25 m	900-1900 m	300-600 m	12 km		
C3 (C3-1)	Lower channel section; before confluence with C3-2	Individual and trains of small to medium sized crescentic-shaped depressions	~10 m	200-300 m	~300m	2 km		
C3 (C3-2)	Channel floor within and following the second bend	Train of large-scale crescentic-shaped depressions	~25 m	1400-3900 m	~700 m	16 km		
C3 (C3-3)	Channel floor before basin 2	Train of large-scale crescentic-shaped depression	20-50 m	500-1500 m	800-1000 m	18 km		

Fig. 9. Location and characteristics of crescentic shaped bedforms that are deeper than the average seafloor found along canyon and channel systems of the western Ionian Basin. Images to the right show morphological examples, sub-bottom profiles (where available) and 2D geomorphological profiles for each bedform. For location of each example (a-e) see Fig. 2B, for location of profiles see dashed black line on morphological image to the left.

grained material or small to medium sized erosional or depositional bedforms as a result of high energy events such as river discharges, storm surges or gravity flows (cf.,Damuth, 1975, 1980; Goswami et al., 2014, 2017). Bedforms of <30 m in size, however, may not be resolved in the bathymetry data due to restrictions in the horizontal resolution (30 m). **Facies B-2** reflections are caused by a diffraction of the acoustic signal often associated with steep slopes and rough morphology such as channel walls and scarps found along **C3** (*c.f.*,Damuth and Olson, 2015).

Facies C and **Facies D** are often associated with low to moderate backscatter patches and are abundant across basins and along channel floors of the southern part of the western Ionian Basin (Figs. 3, 11, 13B). **Facies C** reflections and this type of backscatter intensities can be interpreted as coarse-grained sediments with high silt and sand contents deposited from high velocity currents (Damuth, 1980). We interpret **Facies C**, therefore, as a result of deposition from a diluted debris flow or high-density turbidity current given the distance from potential source areas and distribution of this facies (Fig. 13). Sediment cores collected from regions of **Facies D** contain stacked units of different sediment colour and grain size that are identified as turbidites (Fig. 11) (cf.,Köng et al., 2016; Polonia et al., 2013, 2017; San Pedro et al., 2017). We, therefore, interpret that **Facies D** associated with low to moderate backscatter patches represents stacked turbidites in the research area (e. g., Damuth, 1975, 1980).

Facies E occurs locally throughout the research area in vicinity to steep slopes. This facies is typical for mass transport deposits (MTD) (e. g., Damuth, 1975, 1980). Noticeable is a ~ 10 m-thick sheet-like **Facies E** deposit along the lower slope of **CS2**, which suggests sediment failures along the upper slope (Fig. 13A). The absence of an overlying acoustic facies (**Facies C or D**) indicates fairly recent deposition of this MTD. It is, therefore, likely a result of the last known large event ($M_w > 6$) affecting the region, which was the 1908 earthquake (Rovida et al., 2022). **Facies**

F, which occurs as straight to sinuous ridges and troughs along the present seafloor, is interpreted as sediment waves deposited either from bottom currents or turbidity currents or a combination of both (Figs. 7, 13; 14) (e.g., Damuth and Olson, 2015; Rebesco et al., 2021).

5.2. Indications of past gravity flow activity along different canyon-channel systems

5.2.1. Activity of C1

High backscatter patches indicate high sediment influx from **SiS4**, especially Fiumefreddo Valley, and the Malta Escarpment (Figs. 3D-E). The backscatter patches, however, diminish <25 km downslope from the canyons indicating a limitation in downslope sediment transport (Figs. 3D-E). A subtle change in acoustic facies particularly along the middle and southern part of **C1–1** further indicates a shift from coarser-grained (**Facies A**) to finer-grained sediment (**Facies D**) deposition (Figs. 10, 13) (cf.,Damuth, 1975, 1980). It is interpreted that the width (>2 km-wide) of **C1–1** and, therefore, lack of confinement, causes most gravity flows to quickly lose energy resulting in rapid sediment deposition (cf.,Klaucke et al., 2004; Gavey et al., 2017).

A decrease in the abundance of turbidites within a sequence of downslope sediment cores (KCIR-04, KCIR-01, KCIR-08) supports our finding (Fig. 10). High backscatter patches of **Facies B-1** and **E** along the foot of the Malta Escarpment indicate the deposition of coarse-grained sediment (Fig. 3E, 13) (cf.,Damuth, 1975, 1980). We therefore interpret turbidites found in sediment cores along **C1–1** as a result of sediment failures and consequent gravity flows from Malta Escarpment and Alfeo Seamount rather than from massive gravity flows passing from Mt. Etna through **C1–1** (Fig. 4). These findings are corroborated by findings from Spatola et al. (2020) who showed several large sediment failures across the Malta Escarpment. Sediment waves (**Facies F**) at the foot of
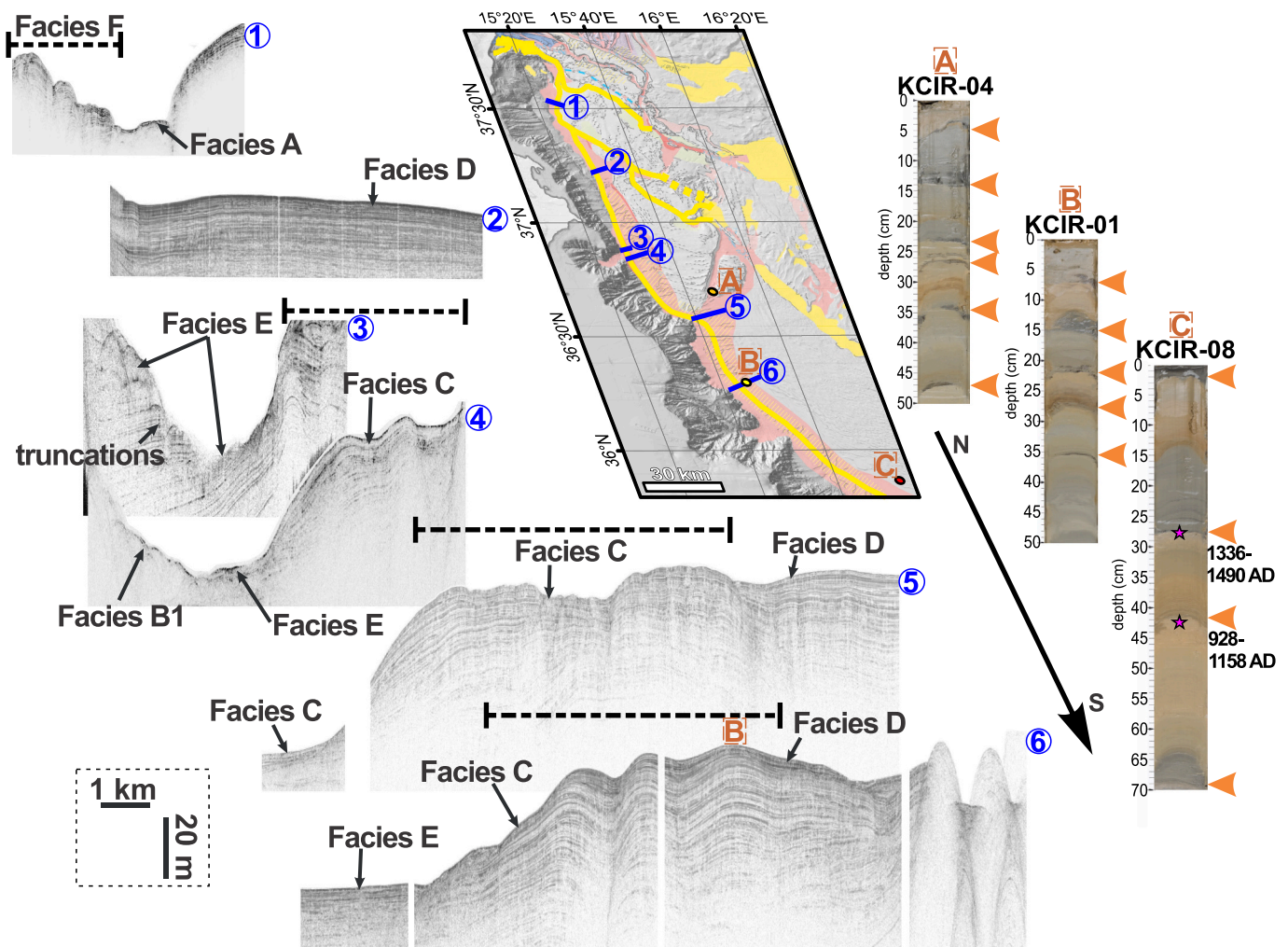
Fig. 10. Sub-bottom profiles showing acoustic facies distribution along **C1**. Profile locations are highlighted by numbers 1–6 and blue bars on the central overview map, all are W-E oriented. The acoustic facies in the uppermost parts of each profile is highlighted. Note: Location of Facies F is shown as dotted line over each profile where present. Circee sediment cores (KCIR04, 01, 08) are displayed on the right and their locations are shown as dots with letters A-C on the overview map. Orientation is downslope, showing a decrease in the abundance of turbidites in the upper 50–70 cm of the cores. Orange arrows show the base of each turbidite, which is in accordance to findings by San San Pedro, 2016. Pink stars show successful attempts of San San Pedro, 2016 to extract samples for dating with ages shown to the right. (For interpretation of the references to colour in this figure legend, the reader is referred to the web version of this article.)

the Malta Escarpment along the southern portion of **C1–1** have been described to be either a result of turbidity or bottom currents (Fig. 4, 13B, 14) (Gutscher et al., 2016; Micallef et al., 2016; Rebesco et al., 2021). Rebesco et al. (2021) interpreted them as a result of bottom currents rather than large-scale turbidity currents given the high bottom current velocities (>10 cm s^{-1}) and absence of progressive downslope thinning and decrease in dimension (Fig. 14). We agree with the observations by Rebesco et al. (2021) and that bottom currents may be the main factor forming these sediment waves. The presence of sediment failures along the Malta Escarpment and abundance of turbidites in sediment cores down to the IAP, however, proofs the occurrence of turbidity currents within **C1–1** (KCIR-04, KCIR-01, KCIR-08) (Polonia et al., 2013, 2017; Köng et al., 2016; San Pedro et al., 2017). It suggests that turbidity currents evolving from these failures may have influenced the development of the sediment waves (**Facies F)** in addition to bottom currents (Figs. 3E, 13B) (cf.,Migeon et al., 2001; e.g., Gutscher et al., 2016). Large-scale gravity flows (>15 km-wide) emerging from an amalgamation of several failures along eastern Sicily and the Malta Escarpment possibly have enough energy to reach the IAP.

5.2.2. Activity of C2

C2 is interpreted as a net-sink for gravity flows rather than a system

that facilitates prolonged sediment transport. It is the only system, however, which is not directly connected to canyons from eastern Sicily or Calabria (Fig. 4). Gravity flows from **C1** and **C3** need to be >30 m-thick in order to bypass the 30 to 60 m-high hanging valleys leading into **C2** (Fig. 6). Sub-bottom profiler data indicate that the upper part of **C2** is dominated by coarser grained sediment material (**Facies C, C2–1)** and up to 20 m-thick MTDs (**Facies E, C2–2 & C2–3)** (Fig. 13B). The sediment appears to be finer grained downslope towards **C1–1** and **C2–4**, as there is a change in acoustic facies from **Facies E** and **C** into **Facies D** (Figs. 11, 13B). Sediment cores from the southern part of **C2–4** contain stacked units of turbidites (Fig. 11) (cf.,Köng et al., 2016; Polonia et al., 2017; San San Pedro, 2016). Seafloor gradients are <0.1° for >20 km along the up to 6 km-wide channel floor (Fig. 6). These findings suggest that gravity flows undergo flow transformation within **C2**. We interpret that the low seafloor gradient, presence of seafloor relief (up to 80 m-high) along the channel floor and absence of confinement decelerate gravity flows entering **C2**, especially those that continue down C2–4 (cf., Talling et al., 2007; Wynn et al., 2012; Gavey et al., 2017). This flow deceleration results in deposition from the flow and consequent flow transformation either from a debris flow or higher density turbidity currents into more dilute turbidity currents (cf.,Damuth, 1975, 1980; Talling et al., 2007).
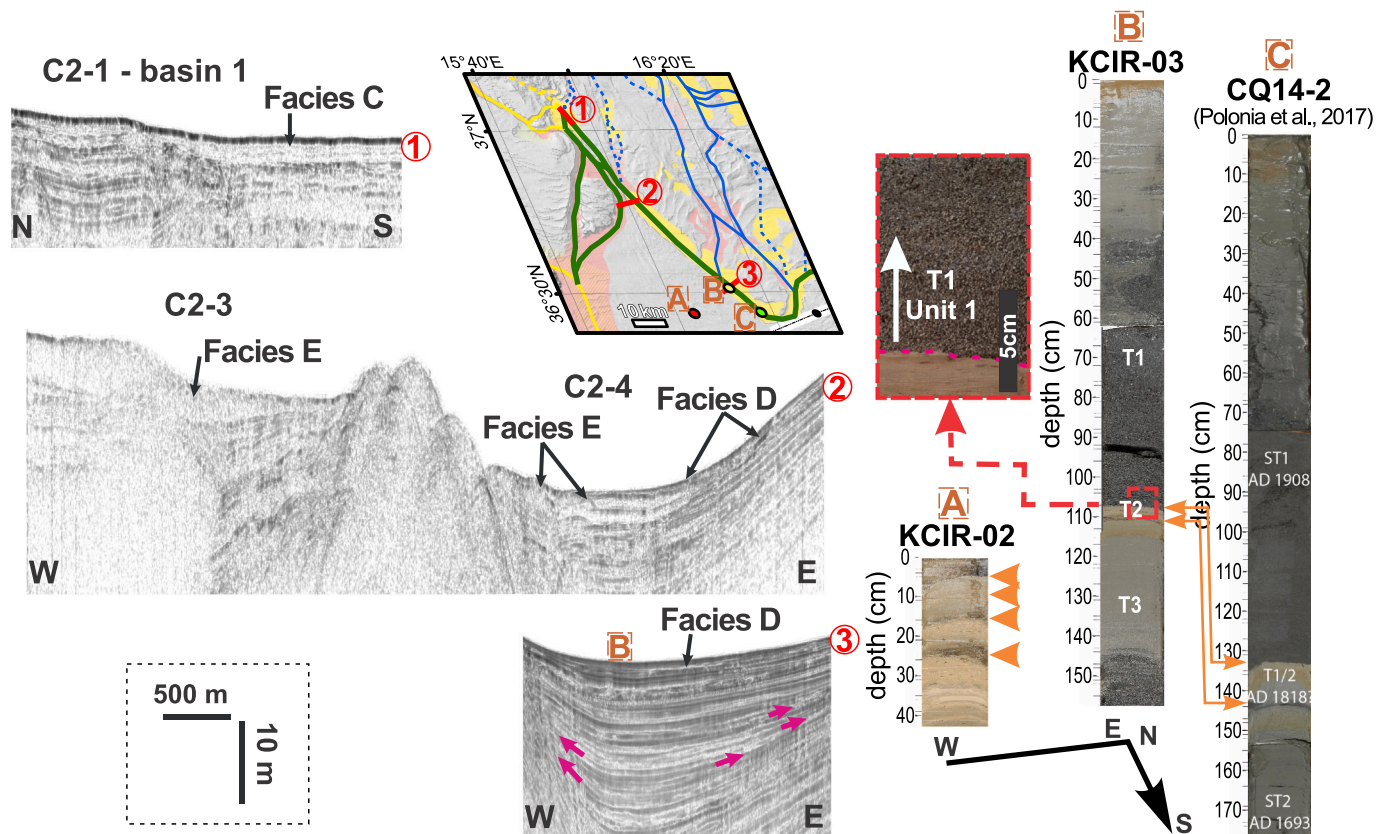
Fig. 11. Sub-bottom profiles showing acoustic facies distribution along **C2** and especially **C2–4**. Location of profiles are highlighted by numbers 1–3 and red bars on the central overview map. The acoustic facies in the uppermost parts of each profile is highlighted. Red arrows in (3) highlight onlapping of reflections towards the basin sides evident in **C2–4**. Circee sediment cores (KCIR02, 03) and CQ14_2 modified from Polonia et al. (2017) are compared to the right. Core locations are shown as dots with letters A-C on the overview map. The base of grey to dark grey sandy units are highlighted with orange arrows. KCIR-03 and CQ14_02 are directly compared as highlighted by orange lines. Zoomed section shows Unit 1 of T1 of KCIR-03. This unit appears as dark grey, coarse sand that shows a high amount of mica. (For interpretation of the references to colour in this figure legend, the reader is referred to the web version of this article.)

Sediment waves (**Facies F**) along **C2–4** with a downslope decrease in dimension are thus interpreted as turbidite sediment waves (Fig. 14) (cf., Rebesco et al., 2021). The ~20 m-high vertical offset along these sediment waves is part of a fault system (Figs. 1A, 14) (e.g., Gutscher et al., 2016). Turbidity currents crossing this offset likely accelerate as a result of hydraulic jumps (cf., Chen et al., 2021). Sediment waves are re-developed at the foot of the fault indicating rapid flow deceleration and consequent sediment deposition (Fig. 14). The MTDs (**Facies E**) apparent along **C2–2** and **C2–3** are interpreted as a result of sediment failures along the Western Lobe or Alfeo Seamount give their location along linear faults of the external CAW (Figs. 1A, 4).

5.2.3. Activity C3

C3 is a highly active system that was likely affected by repeated and recent large-scale gravity flows, as indicated by the abundance of:

1. Straight to sinuous shaped ridges and troughs (**Facies F**) along interchannel heights of **C3–1** and **C3–2**, which are interpreted as turbidite sediment waves (cf., Symons et al., 2016). These net-depositional, upstream migrating cyclic steps are formed by local spillover from gravity flows along unconfined environments (Normark et al., 2002; Fildani et al., 2006; Symons et al., 2016). Their thinning away from the channel suggests sediment spillover from the direction of **C3–2** (cf., Normark et al., 2002; Covault et al., 2017).

2. Trains of crescent-shaped depressions interpreted as large-scale scours (>300 m-long) (cf., Paull et al., 2014; Slootman and Cartigny, 2020).

3. Coarse-grained sediment deposits (**Facies B-1** with high backscatter patches) along the channel floor and in proximity to scours. Validation from sub-bottom profiles in areas with high backscatter patches is not always possible. In these areas high backscatter patches may represent coarse grained material from the deeper sub-bottom rather than the seafloor, given the probability that 12 kHz backscatter data image sediment down to 4 m below the seafloor (Hillman et al., 2018).

4. Localised scarps along channel walls that indicate sediment failures caused either by ground shaking or slope undercutting from bypassing gravity flows (Fig. 8) (e.g., Goswami et al., 2014).

C3 is deeply incised and narrow compared to the other two canyon-channel systems, which allows a relatively long confinement of sediment gravity flows until **basin 2** (Fig. 4). Despite the occurrence of scours (25 m-deep, up to 1.9 km-long) below the confluence with **C1–2**, the overall low backscatter patches and presence of scattered, small to medium sized scours (~10 m-deep, 200–300 m-long) in the lower portion of **C3–1** suggest that this channel was not affected by recent gravity flows (cf., Slootman & Cartney, 2020) (Figs. 3, 9). A higher abundance of erosional and depositional features along **C3–2** such as large-scale trains of scours (~25 m-deep, 1–3.9 km-long) are interpreted either as a result of repeated gravity flow events or a massive and recent gravity flow (Figs. 8, 9). Sediment flows probably quickly decelerate due to the low and unconfined relief of **basin 2**, resulting in deposition of coarse to fine-grained sediments, as indicated by the presence of low and localised high backscatter patches (Fig. 3) (cf., Augustin et al., 1996; Wynn et al., 2012). Only high energy and large gravity flows (>60 m-thick) would be
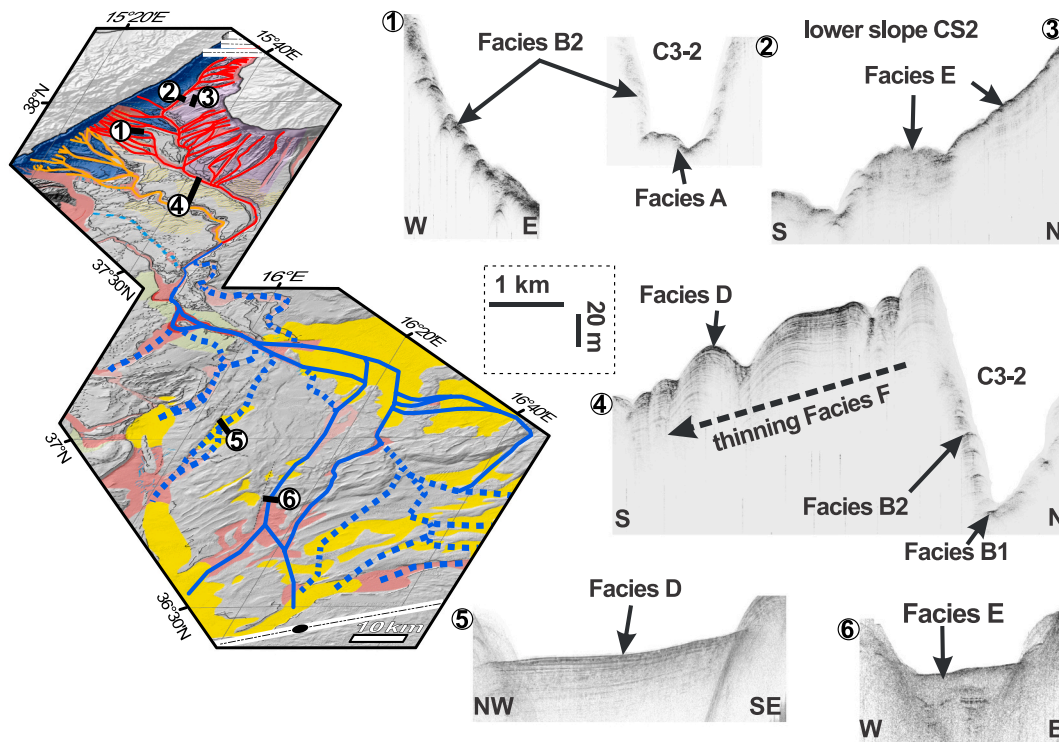
Fig. 12. Sub-bottom profiles showing acoustic facies distribution along **C3**. Location of profiles are highlighted by numbers 1–6 and black bars on the left overview map. The acoustic facies in the uppermost parts of each profile is highlighted. (For interpretation of the references to colour in this figure legend, the reader is referred to the web version of this article.)

able to enter the ~60 m-high hanging valleys that extend downslope from **basin 2** (Fig. 6). It is possible that the increase in slope gradient from **basin 2** (<0.1°) to almost double (<0.2°) within hanging valleys may have been sufficient to cause flow acceleration, erosion and subsequent flow confinement as shown elsewhere (e.g., Wynn et al., 2012). This change in flow behaviour would indicate that the flow was able to keep most of its fine-grained sediment load carrying and depositing it further downslope within **C2–4** and explains the thick mud cap observed on top of KCIR-03 Unit 1 and CQ14_2 Sta1 (Figs. 6, 11) (cf., Wynn et al., 2012). It also would explain the abundance of numerous distributary channels extending downslope from **basin 2** (Fig. 4). The scours within **C3–2** and **C3–3** appear relatively fresh, showing sharp, defined edges that do not appear to be masked by hemipelagic deposition, which indicates that those bedforms were formed or altered by a recent high energy event (Figs. 8; 9) (cf., Paull et al., 2014; Slootman & Cartney, 2020).

5.3. Implications for the 1908 gravity flow

5.3.1. Evidence for the 1908 turbidite in the middle to southern western Ionian Basin

Polonia et al. (2013, 2017, 2021) reported the 1908 turbidite in various sediment cores collected along **C1–1** near the IAP and **C2–4** based on radiocarbon dates (Fig. 2A, e.g., CALA-04, CQ14_02). Turbidites in the CIRCEE-HR cores resemble the turbidites described by Polonia et al. (2013, 2017) (Fig. 11). San San Pedro, 2016 and San Pedro et al. (2017), however, also using radiocarbon dates classified the uppermost turbidite in the CIRCEE-HR cores resulting from either the 1693 southern Sicily earthquake (e.g., KCIR-08) or 1444 Etna eruption (KCIR-02) (Fig. 11). Given the strong similarities (colour, thickness, grain size) and proximity of the KCIR-03 core to the CQ14_02 core of Polonia et al. (2017), we surmise that T1 of KCIR-03 and Sta1 of CQ14_02 may have resulted from the same event (Figs. 2A, 3, 11). We found that the upper deposit in KCIR-02 resembles Unit 1 of KCIR-03. These turbidites are

likely related to 1908 rather than 1693 or 1444, given the proximity to the 1908 cable breaks and the absence of overlying turbidites (Fig. 11) (cf., Ryan and Heezen, 1965; Polonia et al., 2017). If it would indeed be the 1693 deposit, then this would suggest that the 1908 turbidity current was either too powerful, meaning it must have been highly erosional without leaving any deposits within a basin otherwise characterised by long term turbidite deposition, or it took a different passage. Both scenarios are unlikely, as in this case: A) the 1693 deposit would have likely been eroded; and B) cable breaks occurred downslope of these cores, which shows that the gravity flow must have bypassed this location. In addition, the 1444 event is not recorded in any of the cores from Polonia et al. (2013, 2017).

The discrepancy in the age estimates could be associated with uncertainties (e.g., marine reservoir effect, analytical precision, sample contamination) in the radiocarbon dating used by the different groups of researchers (Lowe et al., 2007; Urlaub et al., 2013). In addition, dating of turbidites is often difficult as an undisturbed hemipelagic sample is needed, but may not be available or too thin (<1 cm) between stacked turbidites to allow proper sampling (e.g., Urlaub et al., 2013). Another problem may be that gravity cores not always sample the uppermost sediment layers (Morton and White, 1997; Skinner and McCave, 2003). It could therefore be argued that the 1908 turbidite was not or only partly sampled in the CIRCEE cores (e.g., KCIR-08) and that in both cases the dates are correct. We disregard this scenario for KCIR03, given that the upper 2 m show the same pattern (e.g., number and colour of turbidites) as CQ14_02 (Polonia et al., 2017) (Fig. 11).

5.3.2. The main route of the 1908 gravity flow

The interpreted 1908 turbidite is thickest (up to 1.34 m thick) within **C2–4** and in proximity to the first two cable breaks of the Malta-Zante telegraph cable (Figs. 4, 11) (Ryan and Heezen, 1965; Polonia et al., 2013, 2017; San San Pedro, 2016). This basin is supplied with sediment from both **C1** and **C3** via numerous possible passageways (Fig. 4). **C3** with **C3–2** and **C3–3** was a main passageway for past events as indicated

Legend acoustic facies

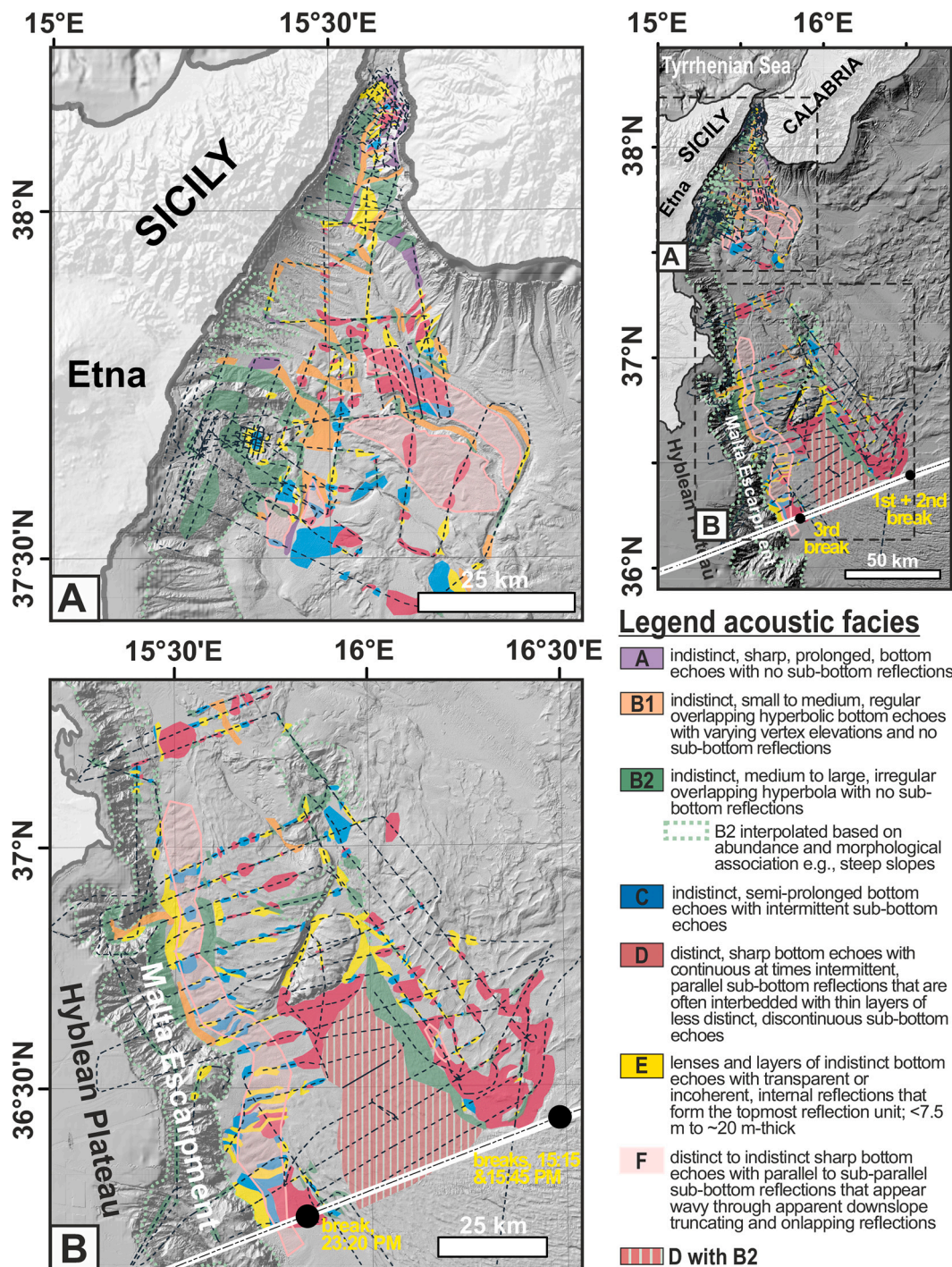| A	indistinct, sharp, prolonged, bottom echoes with no sub-bottom reflections
B1	indistinct, small to medium, regular overlapping hyperbolic bottom echoes with varying vertex elevations and no sub-bottom reflections
B2	indistinct, medium to large, irregular overlapping hyperbola with no sub-bottom reflections
(green dotted)	B2 interpolated based on abundance and morphological association e.g., steep slopes
C	indistinct, semi-prolonged bottom echoes with intermittent sub-bottom echoes
D	distinct, sharp bottom echoes with continuous at times intermittent, parallel sub-bottom reflections that are often interbedded with thin layers of less distinct, discontinuous sub-bottom echoes
E	lenses and layers of indistinct bottom echoes with transparent or incoherent, internal reflections that form the topmost reflection unit; <7.5 m to ~20 m-thick
F	distinct to indistinct sharp bottom echoes with parallel to sub-parallel sub-bottom reflections that appear wavy through apparent downslope truncating and onlapping reflections
D with B2	

Fig. 13. Acoustic facies distribution of the uppermost sub-bottom reflections along the western Ionian Basin based on the classification scheme of Damuth (1975, 1980) and Damuth and Olson (2015). It has to be noted that Facies B-2 covers almost all of the Malta Escarpment and sides along canyons and channels. This facies was not interpolated across these regions, especially the canyon and channel walls, as it would have distracted from the other facies. Black dotted lines show the location of sub-bottom data used within this study. Examples of sub-bottom profiles are shown in Figs. 10-12.

by the abundance of erosional and depositional bedforms (e.g., scours, turbidite sediment waves) (Figs. 4, 6, 8, 9). Although the age of the scours within **C3–2** and upslope of **basin 2** is unknown, they appear fresh, which suggests that they were affected recently by the passage of a large and erosive gravity flow (Figs. 3, 9) (cf.,Paull et al., 2014; Sloot-man & Cartney, 2020). In addition, there are moderate to high back-scatter patches within **basin 2** along paths leading to various hanging valleys. These backscatter patches may be a result of various past gravity flows, but their abundance highlight the activity of **C3** as a passageway

for large sediment flow events. The 1908 event is the most recent known large event in the study area and **C3–3** leads directly to the location of the first two cable breaks (Fig. 4, **C3-cable**) (cf.,Tinti and Armigliato, 2003; Polonia et al., 2013). **C3 (C3–2 & C3–3)** and possible **C2** or parts of it are, therefore, interpreted as the main passageway for the 1908 gravity flow. San San Pedro, 2016 previously suggested similar pas-sageways to the ones presented in this study on the basis of bathymetry and sediment core data, but for events predating 1908. Using XRF and grain size analysis San San Pedro, 2016 and San Pedro et al. (2017)
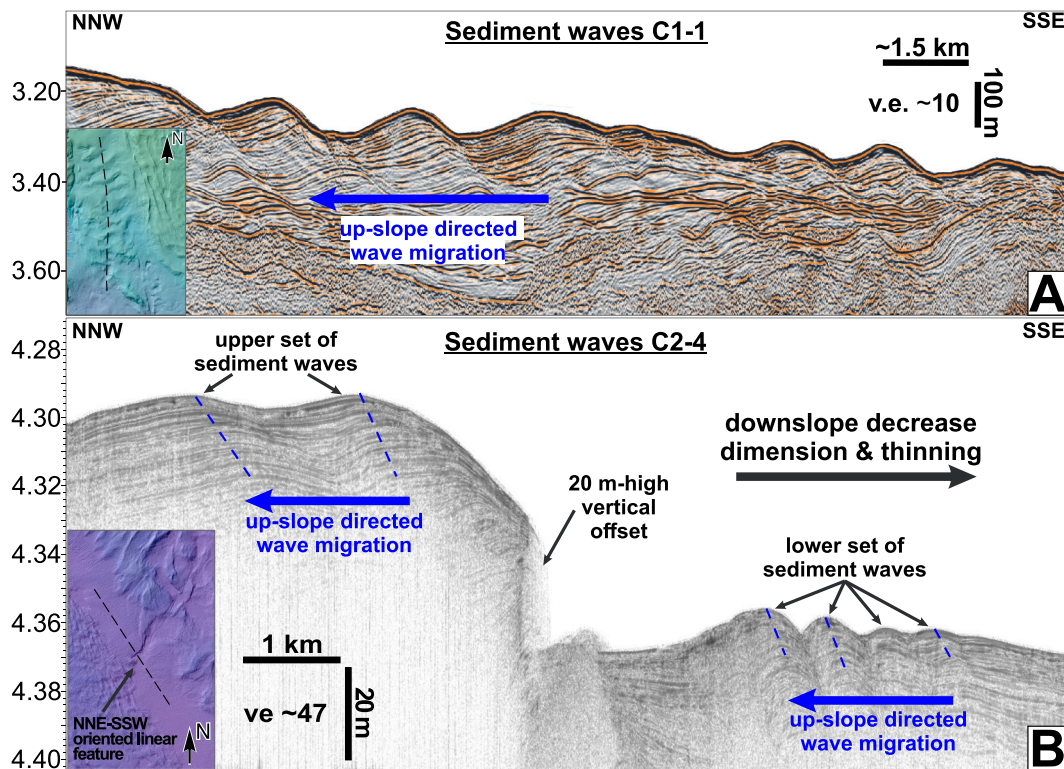
Fig. 14. Comparison of sediment waves apparent in the research area. A) 2D seismic reflection data imaging sediment waves along the southern part of **C1–1**, image modified from Rebesco et al. (2021) and B) Sub-bottom profile showing sediment waves apparent along **C2–4**. Note that in both cases sediment waves tilt upslope as highlighted by the blue dotted lines. (For interpretation of the references to colour in this figure legend, the reader is referred to the web version of this article.)

concluded that past-turbidites in cores from **C2–4** originated from Messina Straits, which supports our interpretation of **C3** as the main passageway.

The cable breaks occurred with a delay of ~30 min suggesting that the gravity flow split across different passageways (). Using the distance from potential source areas (**CS4** and **SiS2**) to the first two cable breaks via **C3** (197 to 222 km) and the timing of the cable breaks (~9 h) provides an average flow velocity of 5.6 to 6.3 ms^{-1} (Figs. 4, 6). It is possible that knickpoints along **C2** and **C3** caused a hydraulic jump with flow acceleration given the sudden change in slope angle and height differences of up to 180 to 300 m (Fig. 6) (cf. Chen et al., 2021). This re-acceleration also may explain that the gravity flow had enough power to cause the cable breaks, despite the potential split along different passageways (cf., Wynn et al., 2012).

The third cable break occurred ~18 h after the earthquake (23:20 pm) and nine hours after the first two cable breaks (Ryan and Heezen, 1965). Different scenarios to explain its occurrence have been put forward:

A. Direct passage from Mt. Etna (**SiS4**) through **C1–1** (Fig. 15B). This scenario would match suggestions by San San Pedro, 2016 and Polonia et al. (2013, 2017), who identified **C1–1** as passageway for 1908 and previous events. It also matches findings from Billi et al. (2008) and Tinti and Armigliato (2003), who suggested a submarine landslide off Fiumefreddo to explain the observed tsunami run-ups. If such a landslide did occur, it would be a likely source for the 1908 gravity flow (e.g., illustrated elsewhere by Piper et al., 1999; Talling et al., 2012: 2013). Seismic reflection data, however, show no indication for a recent landslide within the proposed failure area offshore Fiumefreddo (Argnani et al., 2009b; Gross et al., 2014). Moreover, the distance (~205 km) and the timing of the cable break suggests an average flow velocity of ~3 ms^{-1} (Fig. 6). This velocity would likely be too slow to cause cable breaks (Gavey et al., 2017; Talling et al., 2022).

B. Multiple localised and delayed sediment failures along the Malta Escarpment, the Western Lobe and Alfeo Seamount as a result of aftershocks or the impact of the tsunami wave causing secondary turbidity currents (Fig. 15C). Polonia et al. (2021) previously suggested localised failures along the Malta Escarpment to explain the tsunamite cap found in sediment cores. It is possible that both the tsunami deposit and up to 13 cm-thick sandy unit of the 1908 turbidite that underlies the tsunami unit were caused by these delayed, localised turbidity currents.

C. Overflow of the turbidity current that also caused the first two cable breaks via the external CAW (Fig. 15A). Sub-bottom data (**Facies D**) and turbidites found in KCIR-02 provide evidence that past turbidity currents deposited sediment along large portions of the accretionary wedge and likely also the 1908 turbidite (see 5.3.1, Figs. 11, 13B). The question remains whether a turbidity current crossing the external CAW with its basin-ridge morphology would have still been powerful enough to cause the third cable break (Fig. 15A).

D. The timing of breaks along the Malta-Zante telegraph cable are wrong. This possibility cannot be ignored as the only information about the timing of cable breaks is provided by Ryan and Heezen (1965) with the source about the cable repair stated as "unpublished cable repair records". A change in the sequence of cable breaks could imply that the source for gravity flows along **C1** may have been indeed further upslope and closer to Mt. Etna. A main passage through **C1**, however, contradicts the morphological findings presented in this study, which strongly suggest **C3** as main passageway for the 1908 gravity flow.

5.3.3. Potential source region

North-eastern Sicily and southern Calabria (or portions of it) were previously identified as potential source regions (Ryan and Heezen,
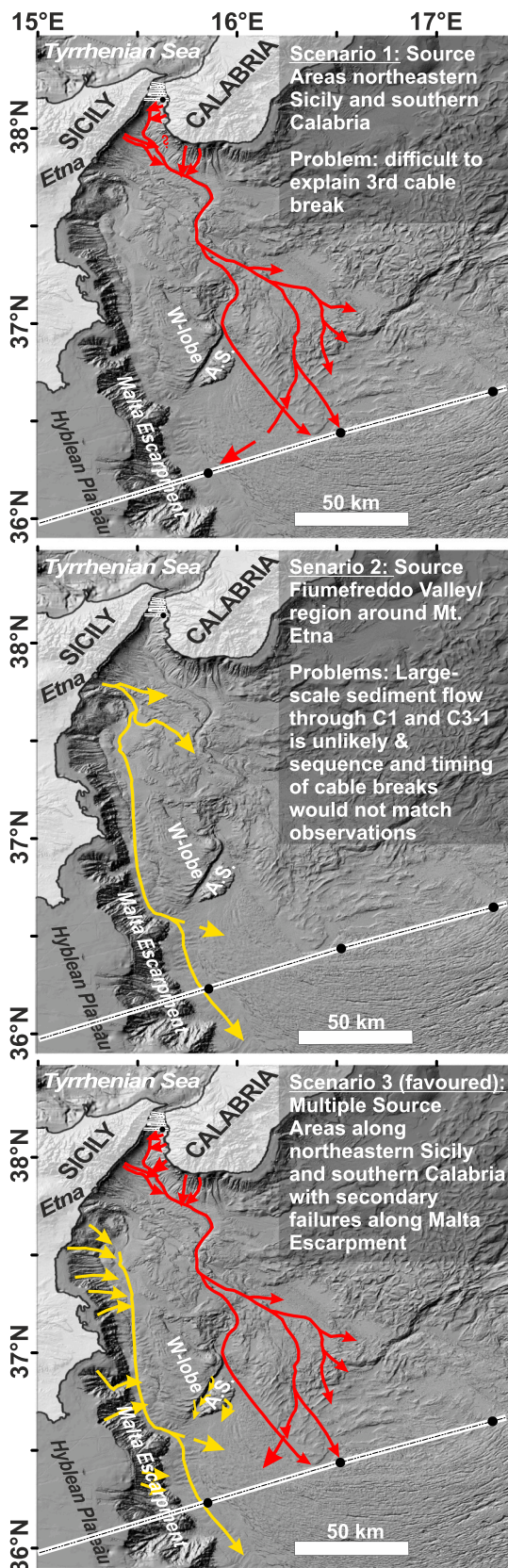
Fig. 15. Different scenarios showing different passageways and source regions for the 1908 gravity flow. Note: Scenario 1 predicts similar source regions and passageways as suggested by San San Pedro, 2016 for the 1693 event leading to deposition in vicinity to the first two cable breaks.

1965; Polonia et al., 2021). Evidence (e.g., high backscatter, acoustic facies distribution) suggest **SiS2, SiS4, CS1** and **CS4** as main passageways for delivering sediment into the western Ionian Basin and indicates recent sediment failure within **CS2** and **CS3** (Figs. 3, 5, 12-13, see 5.1). The different possible source regions show the following characteristics:

1) Canyons floors of **SiS2** show characteristic trains of crescent-shaped bedforms (Figs. 6, 9). These bedforms could be a result of erosion from hyperpycnal river discharge and consequent dilute turbidity currents or sediment destabilisation in 1908 (e.g., Casalbore et al., 2011; Goswami et al., 2014). An absence of sub-bottom and sediment core data, however, does not allow to clearly identify these bedforms (Figs. 2A, 12).

2) **SiS4** canyons merge into **C1–1** and partially **C3–1** via **C1–2** from Fiumefreddo Valley (Fig. 4). **C3–1** shows no indication for the passage of a recent and massive gravity flow, while sediment transport within **C1** appears limited (<25 km) in its downslope extent (Figs. 3D-E, 4). Multiple failures, however, likely occurred along various canyons of the Malta Escarpment (**SiS4**) as a consequence of the impact from the 1908 tsunami or aftershocks (Fig. 15, see 5.3.2) (cf., Arai et al., 2013; Polonia et al., 2017).

3) **CS1** shows numerous scarps resulting from slope failures, which may be potential sources for the 1908 gravity flow (e.g., Goswami et al., 2014). Monaco and Tortorici (2000) reported that the 1908 earthquake caused several landslides between Reggio Calabria and Scilla that are part of the catchment area of **CS1**. The occurrence of numerous landslides onshore may indicate that there were also sediment failures offshore. A cable break offshore Gallico was reported at the time of the earthquake (Fig. 1B) (Ryan and Heezen, 1965). It is further suggested that the 1908 causative fault extends from Messina Straits to the northern part of southern Calabria (**CS1**) (Barreca et al., 2021).

4) The presence of MTDs (**Facies E**) along the lower slope of **CS2** suggests recent sediment failure along the upper slope of **CS2** and **CS3** (Fig. 13B) (see 5.1). This observation is consistent with Goswami et al. (2014), who identified slides within **CS2** and **CS3**, but interpreted high backscatter intensities within **CS2** and **CS3** as bedrock outcrops. Omori (1909) further reported onshore landslides between Pellaro and Lazzaro located within **CS2** and **CS3**. Sparse data coverage along the upper slope of **CS2** and **CS3** does, however, not allow to identify a head scarp.

5) **CS4** shows high backscatter patches but restricted to the canyon floors (Fig. 3B). No major scarp can be identified and the absence of sub-bottom profiles does not allow to indicate any MTDs along the lower slope.

Given above arguments, we interpret that **CS2** and potentially **CS3** are the most likely areas for mass failure in 1908 and thus the most likely main source region for the gravity flow. **CS1** and **CS4** can not be discarded as 1908 source regions given the occurrence of cable breaks within **CS1** and sparse data coverage along **CS4**. The fault system suggested by Barreca et al. (2021) would explain sediment failure along **CS1**, **CS2** and **CS3** as a consequence of the 1908 earthquake. Additional sediment cores from **C3** and further geochemical analysis on existing sediment cores from Messina Straits and the depositional area are needed for a better understanding of the exact source area or areas.

5.3.4. Potential flow thickness and transformation

The height of the backscatter patches within **C3–2** and the presence of overspill turbidite sediment waves on interchannel heights suggest that past sediment flows exceeded a thickness of >170 m within this system (Fig. 6) (cf., Stevenson et al., 2018). We interpret that the 1908 gravity flow was also >170 m-thick given its large run-out and destructive nature >200 km southwards and the distribution of erosional and depositional bedforms (Figs. 7, 9). The presence of scours along **C3–2** further indicates that the 1908 flow must have had already a

suspended upper layer as needed to form these features (Fig. 8) (cf., Slootman & Cartigney, 2020). Scours towards **basin 2** have a similar length to those observed further upslope within **C3–2,** but are more deeply incised, which may imply formation by a more erosive gravity flow (Fig. 9). This finding suggests flow transformation between these two locations. Two scenarios are possible: 1) The gravity flow incorporated coarse-grained sediment from the channel floor turning it into a denser and more erosive flow, which explains the deeper eroded scours (cf.,Covault et al., 2017); or 2) it transformed from a higher density current with a thin turbulent layer into a lower density current with a thicker turbulent layer that somehow had a highly erosive, dense base layer. The gravity flow would have needed to be >60 m-thick to overspill into the hanging valleys surrounding **basin 2** to continue its downslope movement towards the first two cable breaks (Figs. 4, 6). It likely accelerated passing from **basin 2** ($<0.1°$) into the hanging valleys ($<0.2°$) as a result of increased gradients, which allowed it to keep most of its fine-grained sediment load in suspension (Fig. 6) (cf., Wynn et al., 2012). In the vicinity of the first two cable breaks, the turbidity current must have been >140 m-thick in order to reach their location along the external CAW (Fig. 6). It must have been a fully developed turbidity current as evident through turbidites found in sediment cores along **C2–4** (Fig. 11).

A > 60 m-thick gravity flow within **basin 2** indicates that part of the gravity flow entered into **C2** (**C2–1**). The distribution of echo-characteristics (**Facies C** and **E** into **Facies D**) suggests flow transformation from a debris flow or high-density turbidity current into a more dilute turbidity current (Fig. 13) (cf.,Piper et al., 1999). Gradual downstream sediment deposition from the different flow types are evident through the acoustic facies changes and sediment cores collected within the elongated, 6 km-wide and almost flat ($<1°$) basin of **C2–4** (Fig. 11:) (cf., Chen et al., 2021).

6. Conclusions

We identify three main canyon-channel systems within the western Ionian Basin offshore Eastern Sicily; the western (**C1**), central (**C2**) and eastern (**C3**) system. These systems show different activity in terms of sediment transport. **C1** is a highly active system in terms of sediment influx, but transport appears limited <25 km downslope from the canyons due to a lack in confinement along the main channel floor. **C2** is interpreted as the main depositional centre for sediment flows. It shows a long turbidite record. **C3** shows numerous erosional and depositional bedforms (e.g., scours, turbidite sediment waves, channel wall collapse). These bedforms appear fresh, indicating that they were formed or at least altered by a more recent gravity flow event. The last known big event in this region was the 1908 Messina turbidity current. **C3** is therefore interpreted as the main passageway for this gravity flow. It also directly leads to two out of three cable breaks (Ryan and Heezen, 1965). A direct flow from the Mt. Etna area is unlikely given the missing confinement and sequence of cable breaks. Multiple sediment failures along north-eastern Sicily and southern Calabria due to the initial earthquake, and/or secondary failures along Malta Escarpment due to aftershocks or impact from the tsunami wave, are needed to sufficiently explain the sequence of observed cable breaks and distribution of the 1908 turbidite.

The following characteristics about the 1908 gravity flow are derived:

1) *Source region:* Southern Calabria was the most likely source region based on gravity core comparison, morphological characteristics and sub-bottom profile analysis. The Calabrian slope (**CS2, CS3**) off San Leo and Bocale shows up to 10-m thick MTDs along the seafloor, making this area the most likely main source area for 1908. North-eastern Sicily (**SiS2**), however, cannot be fully excluded as additional source region.

2) *Flow thickness:* At least 170 m near the source region, and > 140 m-thick upon reaching the location of the cable breaks.

3) *Flow evolution:* The gravity flow likely already had a suspended second layer near the source area in the upper portion of **C3**, as indicated by the observation of turbidite sediment waves on adjacent interchannel heights. Deeply eroded, large-scale scours (up to 50 m-high, 500–1500 m-long) towards **basin 2** indicate that the gravity flow had potentially evolved into a denser flow such as a debris flow or high-density turbidity current. It is possible that the initial gravity flow incorporated sediment from the channel floor towards **basin 2** ($<0.1°$) turning it into a more erosive flow. The flow potentially also accelerated within subsequent hanging valleys ($<0.2°$) allowing it to carry most of its fine-grained load into **C2–4**. Towards the third cable break the flow must have been a fully developed turbidity current as evident through turbidites found in sediment cores.

4) *Flow velocity:* Estimated to be 5.6 to 6.3 ms^{-1} based on distance to the cable and timing of the breaks, which agree with previous estimates of Ryan and Heezen (1965).

Declaration of Competing Interest

The authors declare that they are not aware of any financial or personal relationships that pose a potential conflict of interest for this reserach.

Data availability

Metadata of the research expeditions (M86–2, CIRCEE-HR, M111, SO277) can be accessed online via Pangaea (https://www.pangaea. de/). The bathymetry data were previously published in Gutscher et al. (2017) and Urlaub et al. (2022). The sub-bottom profiles were acquired during research expedition M86–2 and CIRCEE -HR (Gutscher et al., 2013; Krastel et al., 2014). Sub-bottom profiles and multibeam echosounder data are available through A.M., M.A.G., S.K., M.U. and H. K.. The raw data can be accessed via the following links: https://webapp-srv1a.awi.de/eBathy/batdataset_info.php?idf=803 for M86–2 data (the sub-bottom profiles will be uploaded soon to https://www.pangaea.de/); https://campagnes.flotteoceanographique. fr/campagnes/13020060/ for CIRCEE-HR data; https://www.pangaea. de/?q=campaign:name:%22M111%22 for M111 data; and https://marine-data.de/?site=expedition&expedition=SO277 for SO277 data, which will be available soon via https://www.pangaea.de/. Any other data can be made available upon request to the corresponding author.

References

Amato, A., Azzara, R., Basili, A., Chiarabba, C., Cocco, M., Di Bona, M., Selvaggi, G., 1995. Main Shock and Aftershocks of the December 13, 1990. Eastern Sicily earthquake.

Amblas, D., Ceramicola, S., Gerber, T.P., et al., 2018. Submarine Canyons and Gullies. In: Micallef, A., Krastel, S., Savini, A. (Eds.), Submarine Geomorphology. Springer Geology. Springer, Cham. https://doi.org/10.1007/978-3-319-57852-1_14.

Anzidei, M., Baldi, P., Casula, G., Pondrelli, S., Riguzzi, F., Zanutta, A., 1997. Geodetic and seismological investigation in the Ionian area. Ann. Geophys. 40 (5).

Arai, K., Naruse, H., Miura, R., Kawamura, K., Hino, R., Ito, Y., Inazu, D., Yokokawa, M., Izumi, N., Murayama, M., Kasaya, T., 2013. Tsunami-generated turbidity current of the 2011 Tohoku-Oki earthquake. Geology 41 (11), 1195–1198.

Argnani, A., Brancolini, G., Bonazzi, C., Rovere, M., Accaino, F., Zgur, F., Lodolo, E., 2009a. The results of the Taormina 2006 seismic survey: possible implications for active tectonics in the Messina Straits. Tectonophysics 476 (1–2), 159–169.

Argnani, A., Chiocci, F.L., Tinti, S., Bosman, A., Lodi, M.V., Pagnoni, G., Zaniboni, F., 2009b. Comment on "On the cause of the 1908 Messina tsunami, southern Italy" by Andrea Billi et al. Geophys. Res. Lett. 36, L13307. https://doi.org/10.1029/2009GL037332.

Assier-Rzadkieaicz, S., Heinrich, P., Sabatier, P.C., Savoye, B., Bourillet, J.F., 2000. Numerical modelling of a landslide-generated tsunami: the 1979 Nice event. Pure Appl. Geophys. 157 (10), 1707–1727.

Augustin, J.M., Le Suavé, R., Lurton, X., Voisset, M., Dugelay, S., Satra, C., 1996. Contribution of the multibeam acoustic imagery to the exploration of the sea-bottom. Mar. Geophys. Res. 18 (2), 459–486.

Babonneau, N., Cattaneo, A., Ratzov, G., Déverchère, J., Yelles-Chaouche, A., Lateb, T., Bachir, R.S., 2017. Turbidite chronostratigraphy off Algiers, central Algerian margin: a key for reconstructing Holocene paleo-earthquake cycles. Mar. Geol. 384, 63–80.

Barreca, G., Gross, F., Scarfi, L., Aloisi, M., Monaco, C., Krastel, S., 2021. The Strait of Messina: Seismotectonics and the source of the 1908 earthquake. Earth Sci. Rev. 218, 103685.

Billi, A., Funiciello, R., Minelli, L., Faccenna, C., Neri, G., Orecchio, B., Presti, D., 2008. On the cause of the 1908 Messina tsunami, southern Italy. Geophys. Res. Lett. 35 (6).

Camerlenghi, A., Del Ben, A., Hübscher, C., Forlin, E., Geletti, R., Brancatelli, G., Micallef, A., Saule, M., Facchin, L., 2020. Seismic markers of the Messinian salinity crisis in the deep Ionian Basin. Basin Res. 32 (4), 716–738.

Casalbore, D., Chiocci, F.L., Scarascia Mugnozza, G., Tommasi, P., Sposato, A., 2011. Flash-flood hyperpycnal flows generating shallow-water landslides at Fiumara mouths in Western Messina Strait (Italy). Mar. Geophys. Res. 32 (1), 257–271.

Clare, M., Lintern, D.G., Pope, E., Baker, M., Ruffell, S., Zulkifli, M., Simmons, S., Urlaub, M., Belal, M., Talling, P., 2021. Seismic and Acoustic Monitoring of Submarine Landslides: Ongoing Challenges, Recent Successes and Future Opportunities. EarthArXiv.

Covault, J.A., Kostic, S., Paull, C.K., Ryan, H.F., Fildani, A., 2014. Submarine channel initiation, filling and maintenance from sea-floor geomorphology and morphodynamic modelling of cyclic steps. Sedimentology 61 (4), 1031–1054.

Covault, J.A., Kostic, S., Paull, C.K., Sylvester, Z., Fildani, A., 2017. Cyclic steps and related supercritical bedforms: building blocks of deep-water depositional systems, western North America. Mar. Geol. 393, 4–20.

Damuth, J.E., 1975. Echo character of the western equatorial Atlantic floor and its relationship to the dispersal and distribution of terrigenous sediments. Mar. Geol. 18, 17–45.

Damuth, J.E., 1980. Use of high-frequency (3.5-12 kHz) echograms in the study of near-bottom sedimentation processes in the deep-sea: a review. Mar. Geol. 38, 51–75.

Damuth, J.E., Olson, H.C., 2015. Latest Quaternary sedimentation in the northern Gulf of Mexico Intraslope Basin Province: I. Sediment facies and depositional processes. Geosphere 11 (6), 1689–1718. https://doi.org/10.1130/GES01090.1.

Favalli, M., Boschi, E., Mazzarini, F., Pareschi, M.T., 2009. Seismic and landslide source of the 1908 Straits of Messina tsunami (Sicily, Italy). Geophys. Res. Lett. 36 (16).

Fildani, A., Normark, W.R., Kostic, S., Parker, G., 2006. Channel formation by flow stripping: Large-scale scour features along the Monterey East Channel and their relation to sediment waves. Sedimentology 53 (6), 1265–1287.

Fine, I.V., Rabinovich, A.B., Bornhold, B.D., Thomson, R.E., Kulikov, E.A., 2005. The Grand Banks landslide-generated tsunami of November 18, 1929: preliminary analysis and numerical modeling. Mar. Geol. 215, 45–57.

Gavey, R., Carter, L., Liu, J.T., Talling, P.J., Hsu, R., Pope, E., Evans, G., 2017. Frequent sediment density flows during 2006 to 2015, triggered by competing seismic and weather events: Observations from subsea cable breaks off southern Taiwan. Mar. Geol. 384, 147–158.

Goes, S., Giardini, D., Jenny, S., Hollenstein, C., Kahle, H.G., Geiger, A., 2004. A recent tectonic reorganization in the south-central Mediterranean. Earth Planet. Sci. Lett. 226 (3–4), 335–345.

Goswami, R., Mitchell, N.C., Argnani, A., et al., 2014. Geomorphology of the western Ionian Sea between Sicily and Calabria, Italy. Geo-Mar Lett. 34, 419–433. https://doi.org/10.1007/s00367-014-0374-2.

Goswami, R., Mitchell, N.C., Brocklehurst, S.H., Argnani, A., 2017. Linking subaerial erosion with submarine geomorphology in the western Ionian Sea (south of the Messina Strait), Italy. Basin Res. 29, 641–658.

Gross, F., Krastel, S., Chiocci, F.L., Ridente, D., Bialas, J., Schwab, J., Beier, J., Cukur, D., Winkelmann, D., 2014. Evidence for Submarine Landslides Offshore Mt. Etna, Italy, Submarine Mass Movements and Their Consequences. Springer, Dordrecht, Netherlands, pp. 307–316.

Gutscher, M.-A., Mercier De Lepinay, B., Pinheiro, L., Lefaou, Y., Gallais, F., Dominguez, S., Babonneau, N., Barreca, G., Micallef, A., San Pedro, L., 2013. Circee marine geophysical survey: Ionian Sea (Eastern Sicily - Calabria). SEANOE. https://doi.org/10.17882/49652.

Gutscher, M.-A., Dominguez, S., de Lepinay, B.M., Pinheiro, L., Gallais, F., Babonneau, N., Cattaneo, A., Le Faou, Y., Barreca, G., Micallef, A., Rovere, M., 2016. Tectonic expression of an active slab tear from high-resolution seismic and bathymetric data offshore Sicily (Ionian Sea). Tectonics 35 (1), 39–54.

Gutscher, M.-A., Kopp, H., Krastel, S., Bohrmann, G., Garlan, T., Zaragosi, S., Klaucke, I., Wintersteller, P., Loubrieu, B., Le Faou, Y., San Pedro, L., 2017. Active tectonics of the Calabrian subduction revealed by new multi-beam bathymetric data and high-resolution seismic profiles in the Ionian Sea (Central Mediterranean). Earth Planet. Sci. Lett. 461, 61–72.

Hage, S., Cartigny, M.J., Clare, M.A., Sumner, E.J., Vendettuoli, D., Clarke, J.E.H., Hubbard, S.M., Talling, P.J., Lintern, D.G., Stacey, C.D., Englert, R.G., 2018. How to recognize crescentic bedforms formed by supercritical turbidity currents in the geologic record: Insights from active submarine channels. Geology 46 (6), 563–566.

Hage, S., Cartigny, M.J., Sumner, E.J., Clare, M.A., Hughes Clarke, J.E., Talling, P.J., Lintern, D.G., Simmons, S.M., Silva Jacinto, R., Vellinga, A.J., Allin, J.R., 2019. Direct monitoring reveals initiation of turbidity currents from extremely dilute river plumes. Geophys. Res. Lett. 46 (20), 11310–11320.

Heezen, B.C., Ewing, M., 1952. Turbidity currents and submarine slumps, and the 1929 Grand Banks earthquake. Am. J. Sci. 250, 849–878.

Hillman, J.I., Lamarche, G., Pallentin, A., Pecher, I.A., Gorman, A.R., Schneider von Deimling, J., 2018. Validation of automated supervised segmentation of multibeam backscatter data from the Chatham rise, New Zealand. Mar. Geophys. Res. 39, 205–227.

Hsu, S.K., Kuo, J., Chung-Liang, L., Ching-Hui, T., Doo, W.B., Ku, C.Y., Sibuet, J.C., 2008. Turbidity currents, submarine landslides and the 2006 Pingtung earthquake off SW Taiwan. TAO. Terr. Atmos. Ocean. Sci. 19 (6), 767–772.

Klaucke, I., Masson, D.G., Kenyon, N.H., Gardner, J.V., 2004. Sedimentary processes of the lower Monterey Fan channel and channel-mouth lobe. Mar. Geol. 206 (1–4), 181–198.

Köng, E., Zaragosi, S., Schneider, J.L., Garlan, T., Bachèlery, P., San Pedro, L., Seibert, C., Racine, C., 2016. Untangling the complex origin of turbidite activity on the Calabrian Arc (Ionian Sea) over the last 60 ka. Mar. Geol. 373, 11–25.

Krastel, S., Adami, C., Beier, J., et al., 2014. Seismogenic faults, landslides, and associated tsunamis off southern Italy-Cruise No. M86/2-December 27, 2011-January 17, 2012-Cartagena (Spain)-Brindisi (Italy).

Lowe, J.J., Blockley, S., Trincardi, F., Asioli, A., Cattaneo, A., Matthews, I.P., Pollard, M., Wulf, S., 2007. Age modelling of late Quaternary marine sequences in the Adriatic: towards improved precision and accuracy using volcanic event stratigraphy. Cont. Shelf Res. 27 (3–4), 560–582.

Manik, H.M., Yulius, D., Udrekh, 2015. Development and application of MB system software for bathymetry and seabed computation. Int. J. Softw. Eng. Appl. 9 (6), 143–160.

Meiburg, E., Kneller, B., 2010. Turbidity currents and their deposits. Annu. Rev. Fluid Mech. 42, 135–156.

Micallef, A., Georgiopoulou, A., Mountjoy, J., Huvenne, V.A., Iacono, C.L., Le Bas, T., Del Carlo, P., Otero, D.C., 2016. Outer shelf seafloor geomorphology along a carbonate escarpment: the eastern Malta Plateau, Mediterranean Sea. Cont. Shelf Res. 131, 12–27.

Migeon, S., Savoye, B., Zanella, E., Mulder, T., Faugères, J.C., Weber, O., 2001. Detailed seismic-reflection and sedimentary study of turbidite sediment waves on the Var Sedimentary Ridge (SE France): significance for sediment transport and deposition and for the mechanisms of sediment-wave construction. Mar. Pet. Geol. 18 (2), 179–208.

Monaco, C., Tortorici, L., 2000. Active faulting in the Calabrian arc and eastern Sicily. J. Geodyn. 29 (3–5), 407–424.

Morton, R.A., White, W.A., 1997. Characteristics of and corrections for core shortening in unconsolidated sediments. J. Coast. Res. 761–769.

Mosher, D.C., Moscardelli, L., Shipp, C., Chaytor, J., Baxter, C., Lee, H., Urgeles, R., 2010. Submarine mass movements and their consequences. In: Mosher, D.C., Shipp, R.C., et al. (Eds.), Submarine Mass Movements and Their Consequences, Advances in Natural and Technological Hazards Research, 28. Springer, Dordrecht, pp. 1–10. https://doi.org/10.1007/978-90-481-3071-9.

Mountjoy, J.J., Howarth, J.D., Orpin, A.R., Barnes, P.M., Bowden, D.A., Rowden, A.A., Schimel, A.C., Holden, C., Horgan, H.J., Nodder, S.D., Patton, J.R., 2018. Earthquakes drive large-scale submarine canyon development and sediment supply to deep-ocean basins. Sci. Adv. 4 (3) p. eaar3748.

Normark, W.R., Piper, D.J., Posamentier, H., Pirmez, C., Migeon, S., 2002. Variability in form and growth of sediment waves on turbidite channel levees. Mar. Geol. 192 (1–3), 23–58.

Omori, F., 1909. Preliminary report on the Messina-Reggio earthquake of Dec. 28, 1908. Bull. Imperial Earthq. Investig. Committ. 3 (2), 37–45.

Paull, C.K., Ussler, W.I.I.I., Greene, H.G., Keaten, R., Mitts, P., Barry, J., 2003. Caught in the act: the 20 December 2001 gravity flow event in Monterey Canyon. Geo-Mar. Lett. 22 (4), 227–232.

Paull, C.K., McGann, M., Sumner, E.J., Barnes, P.M., Lundsten, E.M., Anderson, K., Gwiazda, R., Edwards, B., Caress, D.W., 2014. Sub-decadal turbidite frequency during the early Holocene: Eel Fan, offshore northern California. Geology 42 (10), 855–858.

Piper, D.J.W., Cochonat, P., Morrison, M.L., 1999. The sequence of events around the epicentre of the 1929 Grand Banks earthquake: initiation of debris flows and turbidity current inferred from sidescan sonar. Sedimentology 46 (1), 79–97.

Polonia, A., Torelli, L., Mussoni, P., Gasperini, L., Artoni, A., Klaeschen, D., 2011. The Calabrian Arc subduction complex in the Ionian Sea: Regional architecture, active deformation, and seismic hazard. Tectonics 30 (5), TC5018. https://doi.org/10.1029/2010TC00821.

Polonia, A., Panieri, G., Gasperini, L., Gasparotto, G., Bellucci, L.G., Torelli, L., 2013. Turbidite paleoseismology in the Calabrian Arc subduction complex (Ionian Sea). Geochem. Geophys. Geosyst. 14 (1), 112–140.

Polonia, A., Nelson, C.H., Romano, S., Vaiani, S.C., Colizza, E., Gasparotto, G., Gasperini, L., 2017. A depositional model for seismo-turbidites in confined basins based on Ionian Sea deposits. Mar. Geol. 384, 177–198.

Polonia, A., Bonetti, C., Bonetti, J., Çağatay, M.N., Gallerani, A., Gasperini, L., Nelson, C. H., Romano, S., 2021. Deciphering co-seismic sedimentary processes in the Mediterranean sea using elemental, organic carbon, and isotopic data. Geochem. Geophys. Geosyst. 22 (7) p. e2020GC009446.

Rebesco, M., Camerlenghi, A., Munari, V., Mosetti, R., Ford, J., Micallef, A., Facchin, L., 2021. Bottom current-controlled Quaternary sedimentation at the foot of the Malta Escarpment (Ionian Basin, Mediterranean). Mar. Geol. 441, 106596.

Ridente, D., Martorelli, E., Bosman, A., Chiocci, F.L., 2014. High-resolution morpho-bathymetric imaging of the Messina Strait (Southern Italy). New insights on the 1908 earthquake and tsunami. Geomorphology 208, 149–159.

Rovida, A., Locati, M., Camassi, R., Lolli, B., Gasperini, P., Antonucci, A., 2022. Italian Parametric Earthquake Catalogue (CPTI15), Version 4.0. Istituto Nazionale di Geofisica e Vulcanologia (INGV). https://doi.org/10.13127/CPTI/CPTI15.4.

Ryan, W.B.F., Heezen, B.C., 1965. Ionian Sea submarine canyons and the 1908 Messina turbidity current. Geol. Soc. Am. Bull. 76 (8), 915–932.

San Pedro, L., 2016. Title: Déformation de la marge est-sicile et de l'arc Calabrais: étude paléosimologique à travers l'enregistrement sédimentaire des turbidites. Univ. Brest (Université de Bretagne Occidentale), pp. 1–259. PhD thesis.

San Pedro, L., Babonneau, N., Gutscher, M.-A., Cattaneo, A., 2017. Origin and chronology of the Augias deposit in the Ionian Sea (Central Mediterranean Sea), based on new regional sedimentological data. Mar. Geol. 384, 199–213.

Schambach, L., Grilli, S.T., Tappin, D.R., Gangemi, M.D., Barbaro, G., 2020. New simulations and understanding of the 1908 Messina tsunami for a dual seismic and deep submarine mass failure source. Mar. Geol. 421, 106093.

Skinner, L.C., McCave, I.N., 2003. Analysis and modelling of gravity-and piston coring based on soil mechanics. Mar. Geol. 199 (1–2), 181–204.

Slootman, A., Cartigny, M.J., 2020. Cyclic steps: Review and aggradation-based classification. Earth Sci. Rev. 201, 102949.

Sparnocchia, S., Gasparini, G.P., Schroeder, K., Borghini, M., 2011. Oceanographic conditions in the NEMO region during the KM3NeT project (April 2006–May 2009). In: Nuclear Instruments and Methods in Physics Research Section A: Accelerators, Spectrometers, Detectors and Associated Equipment, 626, pp. S87–S90.

Spatola, D., del Moral-Erencia, J.D., Micallef, A., Camerlenghi, A., Garcia-Castellanos, D., Gupta, S., Bohorquez, P., Gutscher, M.-A., Bertoni, C., 2020. A single-stage megaflood at the termination of the Messinian salinity crisis: Geophysical and modelling evidence from the eastern Mediterranean Basin. Mar. Geol. 430, 106337.

Spieß, V., 1993. Digitale Sedimentechographie – Neue Wege zu einer hochauflösenden Akustostratigraphie. Berichte Fachbereich Geowissenschaften Univ. Bremen 35, 1–199.

Stevenson, C.J., Feldens, P., Georgiopoulou, A., Schönke, M., Krastel, S., Piper, D.J., Lindhorst, K., Mosher, D., 2018. Reconstructing the sediment concentration of a giant submarine gravity flow. Nat. Commun. 9 (1), 1–7.

Symons, W.O., Sumner, E.J., Talling, P.J., Cartigny, M.J., Clare, M.A., 2016. Large-scale sediment waves and scours on the modern seafloor and their implications for the prevalence of supercritical flows. Mar. Geol. 371, 130–148.

Talling, P.J., 2014. On the triggers, resulting flow types and frequencies of subaqueous sediment density flows in different settings. Mar. Geol. 352, 155–182.

Talling, P.J., Wynn, R.B., Masson, D.G., Frenz, M., Cronin, B.T., Schiebel, R., Akhmetzhanov, A.M., Dallmeier-Tiessen, S., Benetti, S., Weaver, P.P.E., Georgiopoulou, A., 2007. Onset of submarine debris flow deposition far from original giant landslide. Nature 450 (7169), 541–544.

Talling, P.J., Masson, D.G., Sumner, E.J., Malgesini, G., 2012. Subaqueous sediment density flows: Depositional processes and deposit types. sedimentology 59 (7), 1937–2003.

Talling, P.J., Paull, C.K., Piper, D.J., 2013. How are subaqueous sediment density flows triggered, what is their internal structure and how does it evolve? Direct observations from monitoring of active flows. Earth Sci. Rev. 125, 244–287.

Talling, P.J., Baker, M.L., Pope, E.L., Ruffell, S.C., Jacinto, R.S., Heijnen, M.S., Hage, S., Simmons, S.M., Hasenhündl, M., Heerema, C.J., McGhee, C., 2022. Longest sediment flows yet measured show how major rivers connect efficiently to deep sea. Nat. Commun. 13 (1), 1–15.

Teledyne Marine, 2017. ATLAS PARASOUND Deep-Sea Parametric Sub-Bottom Profiler. http://www.teledynemarine.com/parasound-sub-bottom-profilers?ProductLine ID=79/. Slangerup, Denmark (accessed 21 October 2022).

Tinti, S., Armigliato, A., 2003. The use of scenarios to evaluate the tsunami impact in southern Italy. Mar. Geol. 199 (3–4), 221–243.

Urlaub, M., Talling, P.J., Masson, D.G., 2013. Timing and frequency of large submarine landslides: implications for understanding triggers and future geohazard. Quat. Sci. Rev. 72, 63–82.

Urlaub, M., Geersen, J., Petersen, F., Gross, F., Bonforte, A., Krastel, S., Kopp, H., 2022. The submarine boundaries of Mount Etna's Unstable Southeastern Flank. Front. Earth Sci. 234.

Valensise, G., Pantosti, D., 1992. A 125 Kyr-long geological record of seismic source repeatability: the Messina Straits (southern Italy) and the 1908 earthquake (Ms 7 1/2). Terra Nova 4 (4), 472–483.

Wynn, R.B., Talling, P.J., Masson, D.G., Le Bas, T.P., Cronin, B.T., Stevenson, C.J., 2012. The influence of subtle gradient changes on deep-water gravity flows: a case study from the Moroccan turbidite system. SEPM Spec. Publ. 99, 371–383.